AIMS Mathematics, 9(8): 21356–21382.
DOI: 10.3934/math.20241037
Received: 01 April 2024
Revised: 18 June 2024
Accepted: 21 June 2024
Published: 02 July 2024

https://www.aimspress.com/journal/Math

Research article

On the application of subspace migration from scattering matrix with constant-valued diagonal elements in microwave imaging

Won-Kwang Park*

Department of Information Security, Cryptology, and Mathematics, Kookmin University, Seoul, 02707, Korea

* **Correspondence:** Email: parkwk@kookmin.ac.kr.

Abstract: We apply subspace migration (SM) for fast identification of a small object in microwave imaging. Most research in this area is performed under the assumption that the diagonal elements of the scattering matrix can be easily measured if the transmitter and the receiver are in the same location. Unfortunately, it is very difficult to measure such elements in most real-world microwave imaging. To address this issue, several studies have been conducted with the unknown diagonal elements set to zero. In this paper, we generalize the imaging problem by using SM to set the diagonal elements of the scattering matrix to a constant. To demonstrate the applicability of SM and its dependence on the constant, we show that the imaging function of SM can be represented by an infinite series of Bessel functions of integer order, antenna number and arrangement, and the applied constant. This result allows us to discover additional properties, such as the unique determination of the object. We also demonstrated simulation results using synthetic data to back up the theoretical result.

Keywords: microwave imaging; subspace migration; scattering matrix; Bessel functions; simulation results
Mathematics Subject Classification: 78A46

1. Introduction

There are significant and intriguing inverse problems with retrieving inhomogeneities embedded in a medium under multistatic measurement conditions. This is an old but interesting problem because of its diverse applications, which have a significant impact on human lives. For example, it can be used in biomedical imaging [1, 2], thermal therapy monitoring [3, 4], landmine detection [5, 6], damage detection [7, 8], and radar imaging [9, 10]. To this end, several researchers have investigated and successfully applied various iterative (quantitative) and non-iterative (qualitative) reconstruction algorithms to address inverse scattering and microwave imaging problems.

Some examples of iterative schemes are the Gauss–Newton method for biomedical imaging [11], Born iterative method for brain stroke detection [12] and compressive sensing imaging [13], Levenverg–Marquardt method for parameter distribution reconstruction [14], and level-set method for shape reconstruction [15]. To successfully apply iterative-based algorithms, the iteration procedure must begin with a good initial guess that is close to the true solution. If not, it will be difficult to obtain good results due to the non-convergence issue, local minimizer problem, and demand of large computational costs (see [16, 17] for instance).

Although the non-iterative scheme cannot retrieve complete information on parameter distribution or unknown targets, it can quickly recognize the existence or obtain an outline shape of the target, which can then be used as a good initial guess. For example, the bifocusing method for object detection in microwave imaging [18] and damage detection of civil structure [7], MUltiple SIgnal Classification (MUSIC) algorithm for detecting internal corrosion [19] and object detection in microwave imaging [20], direct sampling method for diffusive optical tomography [21] and electrical impedance tomography [22], topological derivative strategy for ultrasonic non-destructive testing [23] and detection of impedance obstacles [24], orthogonality sampling method for object detection in microwave imaging [25] and 3D objects [26], factorization method for breast cancer imaging [27] and electrical impedance tomography [28], and linear sampling method for underwater acoustic imaging [29] and microwave imaging [30].

In this paper, we investigate the use of subspace migration (SM) to rapidly identify a two-dimensional small object with different dielectric permittivity and electric conductivity values from the background homogeneous medium. SM is a novel and promising non-iterative imaging technique for inverse scattering problems and microwave imaging. It is notable for its speed, accuracy in recognizing target locations and shapes, and robustness to random noise. As a result, SM has been successfully applied to several problems, including localization of small and extended targets [31–33], crack imaging [34–36], and object detection in microwave imaging [37–39].

In designing an imaging function of SM, it is critical to consider the complete elements of the so-called multistatic response matrix in inverse scattering problems and the scattering matrix in microwave imaging. However, in some microwave imaging applications, collecting the diagonal elements of the scattering matrix is difficult due to the difficulty in measuring scattering parameter data (elements of the scattering matrix) or distinguishing weak scattered signals from relatively high antenna reflections when the transmitting and receiving antennas coincide, refer to [4, 39–42] for a detailed discussion on this topic. Therefore, applying SM directly without knowing the diagonal elements of the scattering matrix is difficult. Numerical simulation results show that setting the diagonal elements to a nonzero constant produces poor results. As a result, most studies on microwave imaging problems have used the approach of setting the diagonal elements to zero, refer to [20, 33, 38, 43–46]. However, the theoretical basis for the effect of converting these elements to a constant value remains unknown.

In this study, we consider how SM can be used to quickly identify small object from a scattering matrix with scattering parameter data as its elements. By converting the unknown diagonal elements of the scattering matrix into a fixed constant, we introduce the imaging function of SM and demonstrate that it can be represented by an infinite series of the Bessel function of integer order, total number of antennas and their arrangement, applied frequency, background material properties, and applied constant. Based on the investigated structure of the imaging function, we confirm that the imaging performance is significantly affected by the applied constant, and the object can be identified if the

absolute value of such a constant is zero or close to zero. We present simulation results based on synthetic data to demonstrate the theoretical result.

The rest of the paper is organized as follows. In Section 2, we briefly present the concept of scattering parameters in the presence of a small object and introduce the imaging function of SM from a scattering matrix whose diagonal elements are fixed constants. In Section 3, we build a mathematical theory for the imaging function, discuss its properties, including ideal and practical conditions for good results, and explain the unique determination of the object. Section 4 provides numerical simulation results for single and multiple objects to validate the theoretical result. Section 5 provides a brief conclusion.

2. Scattering parameters and imaging function of the SM

This section briefly introduces the scattering parameters and the imaging function of the SM for identifying a small object D with smooth boundary ∂D. Throughout this paper, we denote Ω as a homogeneous region filled by a matching liquid and Λ_n as an antenna to transmit/receive signals located at $\mathbf{a}_n$ with $|\mathbf{a}_n| = R$, $n = 1, 2, \ldots, N$. We assume that D and Ω are characterized by their dielectric permittivity and electrical conductivity at a given angular frequency $\omega = 2\pi f$, where f denotes the ordinary frequency measured in `hertz`. Correspondingly, the value of the magnetic permeability is set to a constant $\mu(\mathbf{z}) \equiv \mu_{\mathrm{b}} = 4\pi \times 10^{-7}$ H/m for each $\mathbf{z} \in \Omega$. The values of permittivity of Ω and D are represented by ε_{b} and ε_{a}, respectively. Similarly, σ_{b} and σ_{a} represent the values of the conductivity of Ω and D, respectively. With this, we define k_0 and k_{b} as the lossless background and background wavenumbers that satisfy

$$k_0^2 = \omega^2 \varepsilon_{\mathrm{b}} \mu_{\mathrm{b}} \quad \text{and} \quad k_{\mathrm{b}}^2 = \omega^2 \mu_{\mathrm{b}} \left(\varepsilon_{\mathrm{b}} - i \frac{\sigma_{\mathrm{b}}}{\omega} \right),$$

respectively.

Let $\mathcal{S}(n, m)$ be the scattering parameter, defined as the ratio

$$\mathcal{S}(n, m) = \frac{\mathcal{V}_{\mathrm{out}}^{(n)}}{\mathcal{V}_{\mathrm{in}}^{(m)}},$$

where $\mathcal{V}_{\mathrm{in}}^{(m)}$ and $\mathcal{V}_{\mathrm{out}}^{(n)}$ denote the input voltages (or incident waves) at Λ_m and the output voltages (or reflected waves) at Λ_n. We denote $\mathcal{S}_{\mathrm{meas}}(n, m)$ as the measurement data obtained by subtracting scattering parameters with and without D. Then, according to [3], $\mathcal{S}_{\mathrm{meas}}(n, m)$ can be expressed as

$$\mathcal{S}_{\mathrm{meas}}(n, m) = -\frac{ik_0^2}{4\omega\mu_{\mathrm{b}}} \int_D \left(\frac{\varepsilon_{\mathrm{a}} - \varepsilon_{\mathrm{b}}}{\varepsilon_{\mathrm{b}}} + i \frac{\sigma_{\mathrm{a}} - \sigma_{\mathrm{b}}}{\omega \varepsilon_{\mathrm{b}}} \right) \mathbf{E}_{\mathrm{inc}}(\mathbf{a}_m, \mathbf{x}) \cdot \mathbf{E}_{\mathrm{tot}}(\mathbf{x}, \mathbf{a}_n) \mathrm{d}\mathbf{x}, \tag{2.1}$$

where $\mathbf{E}_{\mathrm{inc}}(\mathbf{a}_m, \mathbf{x})$ is the incident field due to the point current density at Λ_m, which satisfies

$$\nabla \times \mathbf{E}_{\mathrm{inc}}(\mathbf{a}_m, \mathbf{x}) = i\omega\mu_{\mathrm{b}} \mathbf{H}(\mathbf{a}_m, \mathbf{x}) \quad \text{and} \quad \nabla \times \mathbf{H}(\mathbf{a}_m, \mathbf{x}) = (\sigma_{\mathrm{b}} - i\omega\varepsilon_{\mathrm{b}}) \mathbf{E}_{\mathrm{inc}}(\mathbf{a}_m, \mathbf{x}),$$

and $\mathbf{E}_{\mathrm{tot}}(\mathbf{x}, \mathbf{a}_n)$ be the total field owing to the presence of the D measured at Λ_n that satisfies

$$\nabla \times \mathbf{E}_{\mathrm{tot}}(\mathbf{x}, \mathbf{a}_n) = i\omega\mu_{\mathrm{b}} \mathbf{H}(\mathbf{x}, \mathbf{a}_n) \quad \text{and} \quad \nabla \times \mathbf{H}(\mathbf{x}, \mathbf{a}_n) = (\sigma(\mathbf{x}) - i\omega\varepsilon(\mathbf{x})) \mathbf{E}_{\mathrm{tot}}(\mathbf{x}, \mathbf{a}_n),$$

with transmission conditions at the boundary ∂D. Here, $\mathbf{H}$ represents the magnetic field and the time-harmonic dependence $e^{-i\omega t}$ is assumed.

Now, assume that the relations

$$\omega\varepsilon_{\mathrm{b}} \gg \sigma_{\mathrm{b}} \quad \text{and} \quad \sqrt{\frac{\varepsilon_{\mathrm{a}}}{\varepsilon_{\mathrm{b}}}}\,\mathrm{diam}(D) < \lambda$$

hold, where $\mathrm{diam}(D)$ and λ represent the diameter of D and the wavelength, respectively. Then, on the basis of [47], it is possible to apply the first-order Born approximation $\mathbf{E}_{\mathrm{tot}}(\mathbf{x}, \mathbf{a}_n) \approx \mathbf{E}_{\mathrm{inc}}(\mathbf{x}, \mathbf{a}_n)$ to (2.1) and, correspondingly, we can observe that

$$\mathcal{S}_{\mathrm{meas}}(n,m) \approx -\frac{ik_0^2}{4\omega\mu_{\mathrm{b}}}\int_D \left(\frac{\varepsilon_{\mathrm{a}}-\varepsilon_{\mathrm{b}}}{\varepsilon_{\mathrm{b}}} + i\frac{\sigma_{\mathrm{a}}-\sigma_{\mathrm{b}}}{\omega\varepsilon_{\mathrm{b}}}\right)\mathbf{E}_{\mathrm{inc}}(\mathbf{a}_m,\mathbf{x})\cdot\mathbf{E}_{\mathrm{inc}}(\mathbf{x},\mathbf{a}_n)\mathrm{d}\mathbf{x}. \tag{2.2}$$

Let us emphasize that, based on the configuration of the microwave machine, only the $z-$component of the incident and total fields can be handled because the antennas are arranged perpendicular to the $z-$axis, see [40, 46]. Then, by letting $z-$component of incident field $\mathbf{E}_{\mathrm{inc}}$ as $\mathrm{E}^{(z)}_{\mathrm{inc}}$ and the reciprocity property of $\mathbf{E}_{\mathrm{inc}}$, (2.2) can be written by

$$\mathcal{S}_{\mathrm{meas}}(n,m) \approx -\frac{ik_0^2}{4\omega\mu_{\mathrm{b}}}\int_D O_D \mathrm{E}^{(z)}_{\mathrm{inc}}(\mathbf{a}_m,\mathbf{x})\mathrm{E}^{(z)}_{\mathrm{inc}}(\mathbf{a}_n,\mathbf{x})\mathrm{d}\mathbf{x}, \tag{2.3}$$

where

$$O_D = \frac{\varepsilon_{\mathrm{a}}-\varepsilon_{\mathrm{b}}}{\varepsilon_{\mathrm{b}}} + i\frac{\sigma_{\mathrm{a}}-\sigma_{\mathrm{b}}}{\omega\varepsilon_{\mathrm{b}}} \quad \text{and} \quad \mathrm{E}^{(z)}_{\mathrm{inc}}(\mathbf{a}_n,\mathbf{x}) = -\frac{i}{4}H_0^{(1)}(k_{\mathrm{b}}|\mathbf{a}_n-\mathbf{x}|). \tag{2.4}$$

Here, $H_0^{(1)}$ denotes the Hankel function of order zero of the first kind.

Next, we will briefly introduce the imaging function of SM. To this end, every element $\mathcal{S}_{\mathrm{meas}}(n,m)$ of the scattering matrix $\mathbb{K}$ must be collected such that

$$\mathbb{K} = \begin{pmatrix} \mathcal{S}_{\mathrm{meas}}(1,1) & \mathcal{S}_{\mathrm{meas}}(1,2) & \cdots & \mathcal{S}_{\mathrm{meas}}(1,N-1) & \mathcal{S}_{\mathrm{meas}}(1,N) \\ \mathcal{S}_{\mathrm{meas}}(2,1) & \mathcal{S}_{\mathrm{meas}}(2,2) & \cdots & \mathcal{S}_{\mathrm{meas}}(1,N-1) & \mathcal{S}_{\mathrm{meas}}(2,N) \\ \vdots & \vdots & \ddots & \vdots & \vdots \\ \mathcal{S}_{\mathrm{meas}}(N,1) & \mathcal{S}_{\mathrm{meas}}(N,2) & \cdots & \mathcal{S}_{\mathrm{meas}}(N,N-1) & \mathcal{S}_{\mathrm{meas}}(N,N) \end{pmatrix}.$$

Following the simulation setup of this study, it is impossible to measure $\mathcal{S}_{\mathrm{meas}}(n,n)$, $n = 1,2,\ldots,N$, because when an antenna Λ_m is used for signal transmission, the remaining $N-1$ antennas Λ_n, $n = 1,2,\ldots,N$ with $n \neq m$ are used for signal reception (see [40] for a further discussion). Thus, we can use the following scattering matrix:

$$\mathbb{K} = \begin{pmatrix} \text{unknown} & \mathcal{S}_{\mathrm{meas}}(1,2) & \cdots & \mathcal{S}_{\mathrm{meas}}(1,N-1) & \mathcal{S}_{\mathrm{meas}}(1,N) \\ \mathcal{S}_{\mathrm{meas}}(2,1) & \text{unknown} & \cdots & \mathcal{S}_{\mathrm{meas}}(1,N-1) & \mathcal{S}_{\mathrm{meas}}(2,N) \\ \vdots & \vdots & \ddots & \vdots & \vdots \\ \mathcal{S}_{\mathrm{meas}}(N,1) & \mathcal{S}_{\mathrm{meas}}(N,2) & \cdots & \mathcal{S}_{\mathrm{meas}}(N,N-1) & \text{unknown} \end{pmatrix}.$$

Consequently, traditional SM cannot be applied directly. Instead, by converting unknown measurement data to a fixed constant, we consider applying the following scattering matrix: given a constant $C \in \mathbb{C}$, let

$$\mathbb{K}(C) = \begin{pmatrix} C & \mathcal{S}_{\text{meas}}(1,2) & \cdots & \mathcal{S}_{\text{meas}}(1,N-1) & \mathcal{S}_{\text{meas}}(1,N) \\ \mathcal{S}_{\text{meas}}(2,1) & C & \cdots & \mathcal{S}_{\text{meas}}(1,N-1) & \mathcal{S}_{\text{meas}}(2,N) \\ \vdots & \vdots & \ddots & \vdots & \vdots \\ \mathcal{S}_{\text{meas}}(N,1) & \mathcal{S}_{\text{meas}}(N,2) & \cdots & \mathcal{S}_{\text{meas}}(N,N-1) & C \end{pmatrix}. \tag{2.5}$$

Since there exists a single small object D, there is only one nonzero singular value, refer to [38]. Thus, the SVD of $\mathbb{K}(C)$ can be written as

$$\mathbb{K}(C) = \sum_{n=1}^{N} \tau_n \mathbf{U}_n \mathbf{V}_n^* \approx \tau_1 \mathbf{U}_1 \mathbf{V}_1^*,$$

where $\mathbf{U}_n$ and $\mathbf{V}_n$ are the left and right singular vectors of $\mathbb{K}(C)$, respectively, and τ_n are the singular values satisfying $\tau_1 > 0$ and $\tau_n \approx 0$ for $n = 2, 3, \ldots, N$. With this, for each search point $\mathbf{z} \in \Omega$, using (2.3) and (2.5), by generating a unit test vector

$$\mathbf{W}(\mathbf{z}) = \frac{1}{\left(\sum_{n=1}^{N} |\mathrm{E}_{\text{inc}}^{(z)}(\mathbf{a}_n, \mathbf{z})|^2\right)^{1/2}} \begin{pmatrix} \mathrm{E}_{\text{inc}}^{(z)}(\mathbf{a}_1, \mathbf{z}) \\ \mathrm{E}_{\text{inc}}^{(z)}(\mathbf{a}_2, \mathbf{z}) \\ \vdots \\ \mathrm{E}_{\text{inc}}^{(z)}(\mathbf{a}_N, \mathbf{z}) \end{pmatrix}, \tag{2.6}$$

the imaging function can be introduced as

$$\mathfrak{F}(\mathbf{z}, C) = |\langle \mathbf{W}(\mathbf{z}), \mathbf{U}_1 \rangle \langle \mathbf{W}(\mathbf{z}), \overline{\mathbf{V}}_1 \rangle|, \quad \text{where} \quad \langle \mathbf{W}(\mathbf{z}), \mathbf{U}_1 \rangle = \mathbf{W}(\mathbf{z})^* \mathbf{U}_1. \tag{2.7}$$

Then, for some particular selection of C, it is possible to recognize $\mathbf{x} \in D$ through the map of $\mathfrak{F}(\mathbf{z}, C)$.

3. Analysis and some intrinsic properties of the imaging function

In this section, we explore the mathematical structure of the imaging function to ensure that the constant C is chosen correctly to produce a good result and discuss some intrinsic properties of the imaging function. The main result is as follows.

Theorem 3.1. *Let $\boldsymbol{\theta}_n = \mathbf{a}_n/R = (\cos\theta_n, \sin\theta_n)$, $\mathbf{z} = |\mathbf{z}|(\cos\varphi, \sin\varphi)$, and $\mathbf{z} - \mathbf{x} = |\mathbf{z} - \mathbf{x}|(\cos\phi, \sin\phi)$. If $|k(\mathbf{z} - \mathbf{a}_n)| \gg 0.25$ for $\mathbf{z} \in \Omega$, then $\mathfrak{F}(\mathbf{z}, C)$ can be represented as follows:*

$$\mathfrak{F}(\mathbf{z}, C) = |\Phi_1(\mathbf{z}) + \Phi_2(\mathbf{z}) + \Phi_3(\mathbf{z}, C)|, \tag{3.1}$$

where

$$\Phi_1(\mathbf{z}) = \frac{N\omega\varepsilon_{\text{b}} e^{2iRk_{\text{b}}} O_D}{32Rk_{\text{b}}\tau_1\pi} \int_D \left(J_0(k_{\text{b}}|\mathbf{z} - \mathbf{x}|) + \frac{1}{N} \sum_{n=1}^{N} \sum_{s \in \overline{\mathbb{Z}}_0} i^s J_s(k_{\text{b}}|\mathbf{z} - \mathbf{x}|) e^{is(\theta_n - \phi)} \right)^2 \mathrm{d}\mathbf{x}$$

$$\Phi_2(\mathbf{z}) = -\frac{\omega\varepsilon_{\mathrm{b}}e^{2iRk_{\mathrm{b}}}O_D}{32Rk_{\mathrm{b}}\tau_1\pi}\int_D\Big(J_0(2k_{\mathrm{b}}|\mathbf{z}-\mathbf{x}|)+\frac{1}{N}\sum_{n=1}^{N}\sum_{s\in\overline{\mathbb{Z}}_0}i^sJ_s(2k_{\mathrm{b}}|\mathbf{z}-\mathbf{x}|)e^{is(\theta_n-\phi)}\Big)\mathrm{d}\mathbf{x}$$

$$\Phi_3(\mathbf{z},C) = \frac{C}{\tau_1}\Big(J_0(2k_{\mathrm{b}}|\mathbf{z}|)+\frac{1}{N}\sum_{n=1}^{N}\sum_{s\in\overline{\mathbb{Z}}_0}i^sJ_s(2k_{\mathrm{b}}|\mathbf{z}|)e^{is\varphi}\Big).$$

Here, J_s is the Bessel function of order s of the first kind and $\overline{\mathbb{Z}}_0 = \mathbb{Z}\cup\{-\infty,+\infty\}\setminus\{0\}$, where $\mathbb{Z}$ represents the set of integer numbers.

Proof. Since $\mathbf{z}\in\Omega$ and $|k(\mathbf{z}-\mathbf{a}_n)|\gg 0.25$ for all n, the Hankel function can be given as the following asymptotic form (see [48, Theorem 2.5] for example)

$$H_0^{(1)}(k_{\mathrm{b}}|\mathbf{z}-\mathbf{a}_n|)\approx\frac{(1+i)e^{ik_{\mathrm{b}}|\mathbf{a}_n|}}{\sqrt{k_{\mathrm{b}}\pi|\mathbf{a}_n|}}e^{-ik_{\mathrm{b}}\boldsymbol{\theta}_n\cdot\mathbf{z}}.$$

By using this representation, we can examine that

$$\mathrm{E}_{\mathrm{inc}}^{(z)}(\mathbf{a}_n,\mathbf{z}) = -\frac{i}{4}H_0^{(1)}(k_{\mathrm{b}}|\mathbf{z}-\mathbf{a}_n|)\approx\frac{(1-i)e^{ik_{\mathrm{b}}|\mathbf{a}_n|}}{4\sqrt{k_{\mathrm{b}}\pi|\mathbf{a}_n|}}e^{-ik_{\mathrm{b}}\boldsymbol{\theta}_n\cdot\mathbf{z}}$$

and

$$\sum_{n=1}^{N}|\mathrm{E}_{\mathrm{inc}}^{(z)}(\mathbf{a}_n,\mathbf{z})|^2\approx\sum_{n=1}^{N}\mathrm{E}_{\mathrm{inc}}^{(z)}(\mathbf{a}_n,\mathbf{z})\overline{\mathrm{E}_{\mathrm{inc}}^{(z)}(\mathbf{a}_n,\mathbf{z})}=\sum_{n=1}^{N}\frac{1}{8k_{\mathrm{b}}\pi|\mathbf{a}_n|}=\frac{N}{8Rk_{\mathrm{b}}\pi}.$$

Thus, the test vector of (2.6) and the measurement data (2.3) can be expressed as

$$\mathbf{W}(\mathbf{z}) = \frac{(1-i)e^{ik_{\mathrm{b}}R}}{\sqrt{2N}}\begin{pmatrix}e^{-ik_{\mathrm{b}}\boldsymbol{\theta}_1\cdot\mathbf{z}}\\ e^{-ik_{\mathrm{b}}\boldsymbol{\theta}_2\cdot\mathbf{z}}\\ \vdots\\ e^{-ik_{\mathrm{b}}\boldsymbol{\theta}_N\cdot\mathbf{z}}\end{pmatrix}$$

and

$$\mathcal{S}_{\mathrm{meas}}(n,m)\approx-\frac{k_0^2e^{2i|\mathbf{a}_n|k_{\mathrm{b}}}O_D}{32|\mathbf{a}_n|k_{\mathrm{b}}\omega\mu_{\mathrm{b}}\pi}\int_D e^{-ik_{\mathrm{b}}(\boldsymbol{\theta}_m+\boldsymbol{\theta}_n)\cdot\mathbf{x}}\mathrm{d}\mathbf{x}:=A\int_D e^{-ik_{\mathrm{b}}(\boldsymbol{\theta}_m+\boldsymbol{\theta}_n)\cdot\mathbf{x}}\mathrm{d}\mathbf{x},$$

respectively. Since

$$\mathbf{U}_1\mathbf{V}_1^* = \frac{1}{\tau_1}\mathbb{K}(C) = \frac{1}{\tau_1}\begin{pmatrix}C & \mathcal{S}_{\mathrm{meas}}(1,2) & \cdots & \mathcal{S}_{\mathrm{meas}}(1,N-1) & \mathcal{S}_{\mathrm{meas}}(1,N)\\ \mathcal{S}_{\mathrm{meas}}(2,1) & C & \cdots & \mathcal{S}_{\mathrm{meas}}(1,N-1) & \mathcal{S}_{\mathrm{meas}}(2,N)\\ \vdots & \vdots & \ddots & \vdots & \vdots\\ \mathcal{S}_{\mathrm{meas}}(N,1) & \mathcal{S}_{\mathrm{meas}}(N,2) & \cdots & \mathcal{S}_{\mathrm{meas}}(N,N-1) & C\end{pmatrix},$$

we can examine that

$$\mathbf{W}(\mathbf{z})^*\mathbf{U}_1\mathbf{V}_1^* = \frac{(1-i)e^{ik_{\mathrm{b}}R}}{\sqrt{2N}\tau_1}\begin{pmatrix}e^{ik_{\mathrm{b}}\boldsymbol{\theta}_1\cdot\mathbf{z}}\\ e^{ik_{\mathrm{b}}\boldsymbol{\theta}_2\cdot\mathbf{z}}\\ \vdots\\ e^{ik_{\mathrm{b}}\boldsymbol{\theta}_N\cdot\mathbf{z}}\end{pmatrix}^T\begin{pmatrix}C & \mathcal{S}_{\mathrm{meas}}(1,2) & \cdots & \mathcal{S}_{\mathrm{meas}}(1,N-1) & \mathcal{S}_{\mathrm{meas}}(1,N)\\ \mathcal{S}_{\mathrm{meas}}(2,1) & C & \cdots & \mathcal{S}_{\mathrm{meas}}(1,N-1) & \mathcal{S}_{\mathrm{meas}}(2,N)\\ \vdots & \vdots & \ddots & \vdots & \vdots\\ \mathcal{S}_{\mathrm{meas}}(N,1) & \mathcal{S}_{\mathrm{meas}}(N,2) & \cdots & \mathcal{S}_{\mathrm{meas}}(N,N-1) & C\end{pmatrix}$$

$$= \frac{(1-i)e^{ik_b R}}{\sqrt{2N}\tau_1} \begin{pmatrix} Ce^{ik_b\boldsymbol{\theta}_1\cdot\mathbf{z}} - \dfrac{k_0^2 e^{2i|\mathbf{a}_n|k_b} O_D}{32|\mathbf{a}_n|k_b\omega\mu_b\pi} \displaystyle\int_D e^{-ik_b\boldsymbol{\theta}_1\cdot\mathbf{x}} \sum_{n\in\mathcal{N}_1} e^{ik_b\boldsymbol{\theta}_n\cdot(\mathbf{z}-\mathbf{x})}\mathrm{d}\mathbf{x} \\ Ce^{ik_b\boldsymbol{\theta}_2\cdot\mathbf{z}} - \dfrac{k_0^2 e^{2i|\mathbf{a}_n|k_b} O_D}{32|\mathbf{a}_n|k_b\omega\mu_b\pi} \displaystyle\int_D e^{-ik_b\boldsymbol{\theta}_2\cdot\mathbf{x}} \sum_{n\in\mathcal{N}_2} e^{ik_b\boldsymbol{\theta}_n\cdot(\mathbf{z}-\mathbf{x})}\mathrm{d}\mathbf{x} \\ \vdots \\ Ce^{ik_b\boldsymbol{\theta}_N\cdot\mathbf{z}} - \dfrac{k_0^2 e^{2i|\mathbf{a}_n|k_b} O_D}{32|\mathbf{a}_n|k_b\omega\mu_b\pi} \displaystyle\int_D e^{-ik_b\boldsymbol{\theta}_N\cdot\mathbf{x}} \sum_{n\in\mathcal{N}_N} e^{ik_b\boldsymbol{\theta}_N\cdot(\mathbf{z}-\mathbf{x})}\mathrm{d}\mathbf{x} \end{pmatrix}^T,$$

where $\mathcal{N}_n = \{1, 2, \ldots, N\} \setminus \{n\}$.

Since the following relation holds uniformly (see [35] for derivation),

$$\begin{aligned} \sum_{n=1}^{N} e^{ik_b\boldsymbol{\theta}_n\cdot(\mathbf{z}-\mathbf{x})} &= \sum_{n=1}^{N} e^{ik_b|\mathbf{z}-\mathbf{x}|\cos(\theta_n-\phi)} = \sum_{n=1}^{N}\left(J_0(k_b|\mathbf{z}-\mathbf{x}|) + \sum_{s\in\overline{\mathbb{Z}}_0} i^s J_s(k_b|\mathbf{z}-\mathbf{x}|)e^{is(\theta_n-\phi)}\right) \\ &= NJ_0(k_b|\mathbf{z}-\mathbf{x}|) + \sum_{n=1}^{N}\sum_{s\in\overline{\mathbb{Z}}_0} i^s J_s(k_b|\mathbf{z}-\mathbf{x}|)e^{is(\theta_n-\phi)} := \mathcal{J}(\mathbf{x},\mathbf{z}), \end{aligned} \tag{3.2}$$

we can obtain

$$\mathbf{W}(\mathbf{z})^*\mathbf{U}_1\mathbf{V}_1^* = \frac{(1-i)e^{ik_b R}}{\sqrt{2N}\tau_1} \begin{pmatrix} Ce^{ik_b\boldsymbol{\theta}_1\cdot\mathbf{z}} + A\displaystyle\int_D e^{-ik_b\boldsymbol{\theta}_1\cdot\mathbf{x}} \sum_{n=1}^{N} e^{ik_b\boldsymbol{\theta}_n\cdot(\mathbf{z}-\mathbf{x})}\mathrm{d}\mathbf{x} - A\displaystyle\int_D e^{-ik_b\boldsymbol{\theta}_1\cdot\mathbf{x}} e^{ik_b\boldsymbol{\theta}_1\cdot(\mathbf{z}-\mathbf{x})}\mathrm{d}\mathbf{x} \\ Ce^{ik_b\boldsymbol{\theta}_2\cdot\mathbf{z}} + A\displaystyle\int_D e^{-ik_b\boldsymbol{\theta}_2\cdot\mathbf{x}} \sum_{n=1}^{N} e^{ik_b\boldsymbol{\theta}_n\cdot(\mathbf{z}-\mathbf{x})}\mathrm{d}\mathbf{x} - A\displaystyle\int_D e^{-ik_b\boldsymbol{\theta}_2\cdot\mathbf{x}} e^{ik_b\boldsymbol{\theta}_2\cdot(\mathbf{z}-\mathbf{x})}\mathrm{d}\mathbf{x} \\ \vdots \\ Ce^{ik_b\boldsymbol{\theta}_N\cdot\mathbf{z}} + A\displaystyle\int_D e^{-ik_b\boldsymbol{\theta}_N\cdot\mathbf{x}} \sum_{n=1}^{N} e^{ik_b\boldsymbol{\theta}_n\cdot(\mathbf{z}-\mathbf{x})}\mathrm{d}\mathbf{x} - A\displaystyle\int_D e^{-ik_b\boldsymbol{\theta}_N\cdot\mathbf{x}} e^{ik_b\boldsymbol{\theta}_N\cdot(\mathbf{z}-\mathbf{x})}\mathrm{d}\mathbf{x} \end{pmatrix}^T$$

$$= \frac{(1-i)e^{ik_b R}}{\sqrt{2N}\tau_1} \begin{pmatrix} Ce^{ik_b\boldsymbol{\theta}_1\cdot\mathbf{z}} + A\displaystyle\int_D e^{-ik_b\boldsymbol{\theta}_1\cdot\mathbf{x}} \mathcal{J}(\mathbf{x},\mathbf{z})\mathrm{d}\mathbf{x} - A\displaystyle\int_D e^{-ik_b\boldsymbol{\theta}_1\cdot\mathbf{x}} e^{ik_b\boldsymbol{\theta}_1\cdot(\mathbf{z}-\mathbf{x})}\mathrm{d}\mathbf{x} \\ Ce^{ik_b\boldsymbol{\theta}_2\cdot\mathbf{z}} + A\displaystyle\int_D e^{-ik_b\boldsymbol{\theta}_2\cdot\mathbf{x}} \mathcal{J}(\mathbf{x},\mathbf{z})\mathrm{d}\mathbf{x} - A\displaystyle\int_D e^{-ik_b\boldsymbol{\theta}_2\cdot\mathbf{x}} e^{ik_b\boldsymbol{\theta}_2\cdot(\mathbf{z}-\mathbf{x})}\mathrm{d}\mathbf{x} \\ \vdots \\ Ce^{ik_b\boldsymbol{\theta}_N\cdot\mathbf{z}} + A\displaystyle\int_D e^{-ik_b\boldsymbol{\theta}_N\cdot\mathbf{x}} \mathcal{J}(\mathbf{x},\mathbf{z})\mathrm{d}\mathbf{x} - A\displaystyle\int_D e^{-ik_b\boldsymbol{\theta}_N\cdot\mathbf{x}} e^{ik_b\boldsymbol{\theta}_N\cdot(\mathbf{z}-\mathbf{x})}\mathrm{d}\mathbf{x} \end{pmatrix}^T$$

and, correspondingly,

$$\mathbf{W}(\mathbf{z})^*\mathbf{U}_1\mathbf{V}_1^*\overline{\mathbf{W}}(\mathbf{z}) = \frac{1}{\tau_1 N}\begin{pmatrix} Ce^{ik_b\boldsymbol{\theta}_1\cdot\mathbf{z}} + A\int_D e^{-ik_b\boldsymbol{\theta}_1\cdot\mathbf{x}}\mathcal{J}(\mathbf{x},\mathbf{z})\mathrm{d}\mathbf{x} - A\int_D e^{-ik_b\boldsymbol{\theta}_1\cdot\mathbf{x}}e^{ik_b\boldsymbol{\theta}_1\cdot(\mathbf{z}-\mathbf{x})}\mathrm{d}\mathbf{x} \\ Ce^{ik_b\boldsymbol{\theta}_2\cdot\mathbf{z}} + A\int_D e^{-ik_b\boldsymbol{\theta}_2\cdot\mathbf{x}}\mathcal{J}(\mathbf{x},\mathbf{z})\mathrm{d}\mathbf{x} - A\int_D e^{-ik_b\boldsymbol{\theta}_2\cdot\mathbf{x}}e^{ik_b\boldsymbol{\theta}_2\cdot(\mathbf{z}-\mathbf{x})}\mathrm{d}\mathbf{x} \\ \vdots \\ Ce^{ik_b\boldsymbol{\theta}_N\cdot\mathbf{z}} + A\int_D e^{-ik_b\boldsymbol{\theta}_1\cdot\mathbf{x}}\mathcal{J}(\mathbf{x},\mathbf{z})\mathrm{d}\mathbf{x} - A\int_D e^{-ik_b\boldsymbol{\theta}_N\cdot\mathbf{x}}e^{ik_b\boldsymbol{\theta}_N\cdot(\mathbf{z}-\mathbf{x})}\mathrm{d}\mathbf{x} \end{pmatrix}^T \begin{pmatrix} e^{ik_b\boldsymbol{\theta}_1\cdot\mathbf{z}} \\ e^{ik_b\boldsymbol{\theta}_2\cdot\mathbf{z}} \\ \vdots \\ e^{ik_b\boldsymbol{\theta}_N\cdot\mathbf{z}} \end{pmatrix}$$
$$= \frac{1}{\tau_1 N}\sum_{n=1}^{N}\left(Ce^{2ik_b\boldsymbol{\theta}_n\cdot\mathbf{z}} + A\int_D e^{ik_b\boldsymbol{\theta}_n\cdot(\mathbf{z}-\mathbf{x})}\mathcal{J}(\mathbf{x},\mathbf{z})\mathrm{d}\mathbf{x} - A\int_D e^{2ik_b\boldsymbol{\theta}_n\cdot(\mathbf{z}-\mathbf{x})}\mathrm{d}\mathbf{x}\right).$$

Now, by applying (3.2) again, we can derive

$$\begin{aligned}\langle\mathbf{W}(\mathbf{z}),\mathbf{U}_1\rangle\langle\mathbf{W}(\mathbf{z}),\overline{\mathbf{V}}_1\rangle &= \mathbf{W}(\mathbf{z})^*\mathbf{U}_1\mathbf{V}_1^*\overline{\mathbf{W}}(\mathbf{z}) \\ &= \frac{C}{\tau_1 N}\sum_{n=1}^{N}e^{2ik_b\boldsymbol{\theta}_n\cdot\mathbf{z}} + \frac{A}{\tau_1 N}\int_D\mathcal{J}(\mathbf{x},\mathbf{z})\sum_{n=1}^{N}e^{ik_b\boldsymbol{\theta}_n\cdot(\mathbf{z}-\mathbf{x})}\mathrm{d}\mathbf{x} - \frac{A}{\tau_1 N}\int_D\sum_{n=1}^{N}e^{2ik_b\boldsymbol{\theta}_N\cdot(\mathbf{z}-\mathbf{x})}\mathrm{d}\mathbf{x} \\ &= \frac{A}{\tau_1 N}\int_D\left(NJ_0(k_b|\mathbf{z}-\mathbf{x}|) + \sum_{n=1}^{N}\sum_{s\in\overline{\mathbb{Z}}_0}i^sJ_s(k_b|\mathbf{z}-\mathbf{x}|)e^{is(\theta_n-\phi)}\right)^2\mathrm{d}\mathbf{x} \\ &\quad - \frac{A}{\tau_1 N}\int_D\left(NJ_0(2k_b|\mathbf{z}-\mathbf{x}|) + \sum_{n=1}^{N}\sum_{s\in\overline{\mathbb{Z}}_0}i^sJ_s(2k_b|\mathbf{z}-\mathbf{x}|)e^{is(\theta_n-\phi)}\right)\mathrm{d}\mathbf{x} \\ &\quad + \frac{C}{\tau_1 N}\left(NJ_0(2k_b|\mathbf{z}|) + \sum_{n=1}^{N}\sum_{s\in\overline{\mathbb{Z}}_0}i^sJ_s(2k_b|\mathbf{z}|)e^{is\varphi}\right).\end{aligned}$$

This gives us the structure of (3.1). □

Based on Theorem 3.1, we can explain some imaging function properties and phenomena that can occur in simulation results.

Remark 3.1 (Impact of the constant C and its best selection). Because $\Phi_3(\mathbf{z}, C)$ lacks information about $\mathbf{x} \in D$, this factor contributes to the generation of several artifacts, which disrupts the detection of D. This means that using a nonzero constant C will make it difficult to retrieve the object via the map of $\mathfrak{F}(\mathbf{z}, C)$, so choosing $C = 0$ will ensure good imaging results. This is the theoretical reason why most studies set the unknown diagonal elements of the scattering matrix to zero. In this case, since $\mathfrak{F}(\mathbf{z}, 0) \approx 1$ when $\mathbf{z} \in D$,

$$\mathfrak{F}(\mathbf{z},0) \approx \left|\frac{N\omega\varepsilon_b e^{2iRk_b}O_D}{32Rk_b\tau_1\pi}\,\mathrm{area}(D) - \frac{\omega\varepsilon_b e^{2iRk_b}O_D}{32Rk_b\tau_1\pi}\,\mathrm{area}(D)\right| \approx 1.$$

Correspondingly, $\mathfrak{F}(\mathbf{z}, 0)$ can be represented as

$$\mathfrak{F}(\mathbf{z},0) \approx \frac{N}{(N-1)\,\mathrm{area}(D)} \int_D \left(J_0(k_\mathrm{b}|\mathbf{z}-\mathbf{x}|) + \frac{1}{N}\sum_{n=1}^{N}\sum_{s\in\overline{\mathbb{Z}}_0} i^s J_s(k_\mathrm{b}|\mathbf{z}-\mathbf{x}|) e^{is(\theta_n-\phi)} \right)^2 \mathrm{d}\mathbf{x}$$
$$- \frac{1}{(N-1)\,\mathrm{area}(D)} \int_D \left(J_0(2k_\mathrm{b}|\mathbf{z}-\mathbf{x}|) + \frac{1}{N}\sum_{n=1}^{N}\sum_{s\in\overline{\mathbb{Z}}_0} i^s J_s(2k_\mathrm{b}|\mathbf{z}-\mathbf{x}|) e^{is(\theta_n-\phi)} \right) \mathrm{d}\mathbf{x}.$$

This result is the same as in [38]. Thus, we can say that Theorem 3.1 can be considered as a generalized version of the previous study.

Remark 3.2 (Detectability of the object). Assume that $C = 0$. Then, since $\Phi_1(\mathbf{z})$ and $\Phi(\mathbf{z})$ have factors $J_0(k_\mathrm{b}|\mathbf{z}-\mathbf{x}|)$ and $J_0(2k_\mathrm{b}|\mathbf{z}-\mathbf{x}|)$, respectively, and $J_0(0) = 1$, the map of $\mathfrak{F}(\mathbf{z},0)$ will contain a peak of large magnitude when $\mathbf{z} = \mathbf{x} \in D$, allowing recognition of the existence, location, and outline shape of object D.

Remark 3.3 (Ideal conditions for good results). According to Remarks 3.1 and 3.2, it will be possible to obtain good results when $\Phi_3(\mathbf{z}, C) = 0$, i.e., $C = 0$,

$$\frac{1}{N}\sum_{n=1}^{N}\sum_{s\in\overline{\mathbb{Z}}_0} i^s J_s(k_\mathrm{b}|\mathbf{z}-\mathbf{x}|) e^{is(\theta_n-\phi)} = 0, \quad \text{and} \quad \frac{1}{N}\sum_{n=1}^{N}\sum_{s\in\overline{\mathbb{Z}}_0} i^s J_s(2k_\mathrm{b}|\mathbf{z}-\mathbf{x}|) e^{is(\theta_n-\phi)} = 0. \tag{3.3}$$

The easiest and simplest method is to select $N \longrightarrow +\infty$; however, this approach is impossible given the simulation situation. Since the following asymptotic form holds for large z,

$$J_s(z) = \sqrt{\frac{2}{\pi z}} \cos\left(z - \frac{s\pi}{2} - \frac{\pi}{4} \right) \quad \text{implies} \quad J_s(k_\mathrm{b}|\mathbf{z}-\mathbf{x}|) \propto \sqrt{\frac{2}{k_\mathrm{b}\pi|\mathbf{z}-\mathbf{x}|}},$$

it will be possible to make $J_s(k_\mathrm{b}|\mathbf{z}-\mathbf{x}|)$, $J_s(2k_\mathrm{b}|\mathbf{z}-\mathbf{x}|) \longrightarrow 0$ when $|k_\mathrm{b}| \longrightarrow +\infty$, or equivalently $f \longrightarrow +\infty$. However, using infinite-valued frequency is impossible in practice. Based on these examinations, we can conclude that if the total number N is small or the applied frequency f is low, it will be difficult to identify the object D.

Remark 3.4 (Practical condition for achieving good results). Here, we consider finding a condition that satisfies the following relation: for $C = 0$, $x \neq 0$, and sufficiently large L,

$$\mathcal{E}(x, L) = \sum_{n=1}^{N}\sum_{s=-L, s\neq 0}^{L} i^s J_s(x) e^{is(\theta_n-\phi)} \approx 0.$$

If $N = 16$ and all antennas are uniformly distributed on a circle of radius R, as shown in Figure 1 of Section 4, then $\mathcal{E}(x, L) \approx 0$ for small L, according to [39]. If L is sufficiently large, then since $J_{-L}(x) = (-1)^L J_L(x)$ and the following relationship holds (see [49] for instance),

$$|J_L(x)| \leq \frac{b}{\sqrt[3]{L}}, \quad b = 0.674885\ldots,$$

the value of $\mathcal{E}(x, L)$ can be disregarded. Table 1 shows the values of $|\mathcal{E}(x, L)|$ for different x and L. This is the theoretical reason for using a uniformly distributed antenna arrangement in most studies.

Following Remarks 3.1, 3.2, 3.3, and 3.4, we can achieve the following result of unique identification.

	$L = 1$	$L = 3$	$L = 5$	$L = 10$	$L \geq 15$
$x = 0.1$	1.5266×10^{-16}	1.3877×10^{-16}	1.8049×10^{-16}	2.2053×10^{-16}	2.2053×10^{-16}
$x = 0.3$	3.3307×10^{-16}	3.1772×10^{-16}	4.8908×10^{-16}	3.1406×10^{-16}	3.0425×10^{-16}
$x = 0.5$	5.5511×10^{-17}	4.6230×10^{-16}	7.4906×10^{-16}	7.9050×10^{-16}	6.6733×10^{-16}
$x = 0.7$	3.3307×10^{-16}	9.8275×10^{-16}	5.5563×10^{-16}	9.3646×10^{-16}	7.0292×10^{-16}
$x = 1.0$	5.5511×10^{-16}	2.1957×10^{-16}	4.6286×10^{-16}	1.5563×10^{-16}	1.6795×10^{-16}

Table 1. (Remark 3.4) Values of $|\mathcal{E}(x, L)|$ for various x and L.

Corollary 3.1 (Unique identification of the object)**.** *Assume that N is an even number greater than* 8 *and that all antennas Λ_n, $n = 1, 2, \ldots, N$, are uniformly distributed on a circle with radius R. Then, for sufficiently high frequency of operation f, the object D can be retrieved uniquely through the maps of $\mathfrak{F}(\mathbf{z}, 0)$.*

4. Simulation results with synthetic and experimental data

4.1. Simulation results with synthetic data

In this section, we present simulation results that demonstrate the theoretical result. To run the simulation, we set the position of the dipole antennas for $n = 1, 2, \ldots, N(= 16)$,

$$\mathbf{a}_n = 0.09\,\text{m}\,(\cos\theta_n, \sin\theta_n)\,, \quad \theta_n = \frac{3\pi}{2} - \frac{2\pi(n-1)}{N}.$$

The ROI Ω was defined as the interior of a square region $(-0.08\,\text{m}, 0.08\,\text{m})^2$ with material properties $(\varepsilon_\text{b}, \sigma_\text{b}) = (20\varepsilon_0, 0.2\,\text{S/m})$ with $f = 1\,\text{GHz}$. Here, $\varepsilon_0 = 8.854 \times 10^{-12}\,\text{F/m}$ represents vacuum permittivity. We chose two balls D_1 and D_2 as objects with the same radii $\alpha = 0.01\,\text{m}$, centers $\mathbf{x}_1 = (0.01\,\text{m}, 0.03\,\text{m})$ and $\mathbf{x}_2 = (-0.04\,\text{m}, -0.02\,\text{m})$, and material properties $(\varepsilon_1, \sigma_1) = (55\varepsilon_0, 1.2\,\text{S/m})$ and $(\varepsilon_2, \sigma_2) = (45\varepsilon_0, 1.0\,\text{S/m})$. Figure 1 shows the simulation settings both without and with objects.

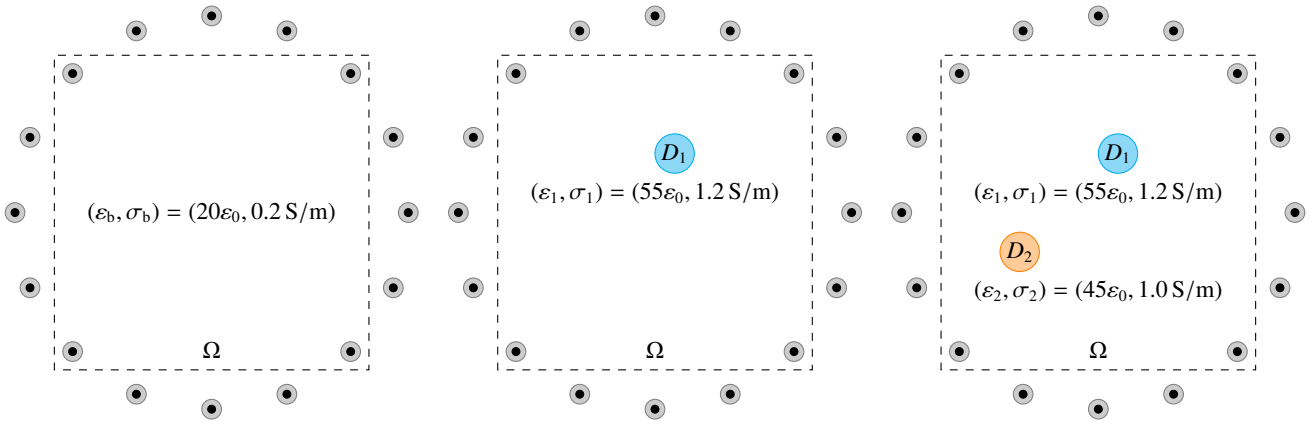

Figure 1. Illustration of the background (left), single (center), and multiple (right) small objects.

Example 4.1 (Imaging of single object). In this example, we focus on imaging of a single object D_1. Figure 2 shows the distribution of singular values of $\mathbb{K}(C)$ for different C. Notice that we can easily distinguish nonzero singular values τ_1 when $C = 0$, 0.01, $0.001i$, and $0.01i$. However, if the value of $|C|$ is not near zero, it is difficult to distinguish between nonzero and near zero singular values, such as $C = 0.1$ and $C = 0.1i$. Fortunately, considering differences $\tau_n - \tau_{n+1}$, $n = 1, 2, \ldots, 15$, we selected τ_1 as the nonzero singular value of $\mathbb{K}(C)$ and defined the imaging function $\mathfrak{F}(\mathbf{z}, C)$ of (2.7).

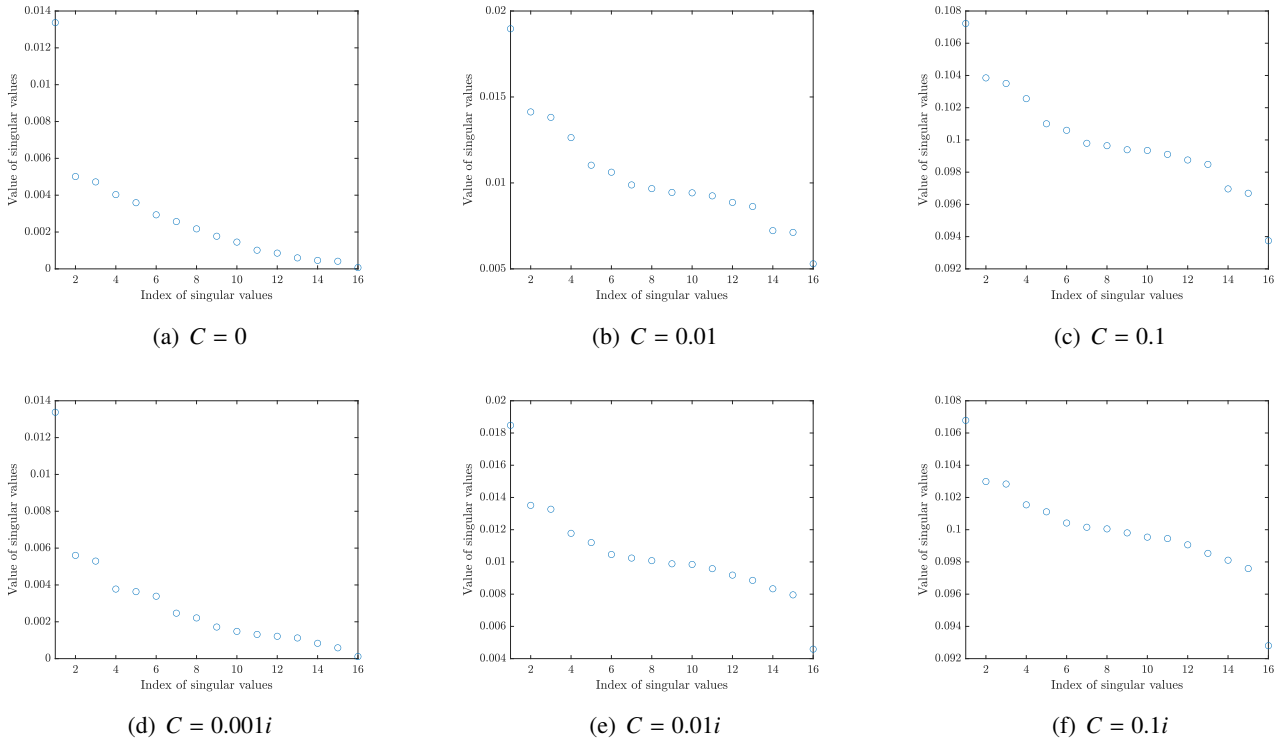

(a) $C = 0$ (b) $C = 0.01$ (c) $C = 0.1$

(d) $C = 0.001i$ (e) $C = 0.01i$ (f) $C = 0.1i$

Figure 2. (Example 4.1) Distribution of the singular values of $\mathbb{K}(C)$ at $f = 1\,\text{GHz}$ with various C.

Figure 3 displays the maps of $\mathfrak{F}(\mathbf{z}, C)$ for different C. Note that if $C = 0$ or $|C|$ is small ($|C| \leq 0.01$), we can precisely identify the existence, location, and shape of D_1 via the map of $\mathfrak{F}(\mathbf{z}, C)$. Meanwhile, it is difficult to distinguish D_1 from an artifact with large magnitude at $(-0.01\,\text{m}, -0.03\,\text{m})$ if $C = 0.1$. Although some artifacts are present in the imaging result, D_1 can be identified because the magnitudes of the artifacts are small when $C = 0.1i$. Thus, we can conclude that the imaging result of $\mathfrak{F}(\mathbf{z}, C)$ is significantly dependent on the choice of C. Furthermore, good results can be obtained when $C = 0$ or $|C|$ is sufficiently small ($|C| \leq 0.01$ in this example) for identifying a single object.

Example 4.2 (Imaging of multiple objects). Now, we use the imaging function $\mathfrak{F}(\mathbf{z}, C)$ to identify multiple small objects D_1 and D_2. In this case, since the SVD of $\mathbb{K}(C)$ is

$$\mathbb{K}(C) = \sum_{n=1}^{N} \tau_n \mathbf{U}_n \mathbf{V}_n^* \approx \sum_{n=1}^{2} \tau_n \mathbf{U}_n \mathbf{V}_n^*,$$

the imaging function of (2.7) becomes

$$\mathfrak{F}(\mathbf{z}, C) = \left| \sum_{n=1}^{2} \langle \mathbf{W}(\mathbf{z}), \mathbf{U}_n \rangle \langle \mathbf{W}(\mathbf{z}), \overline{\mathbf{V}}_n \rangle \right|.$$

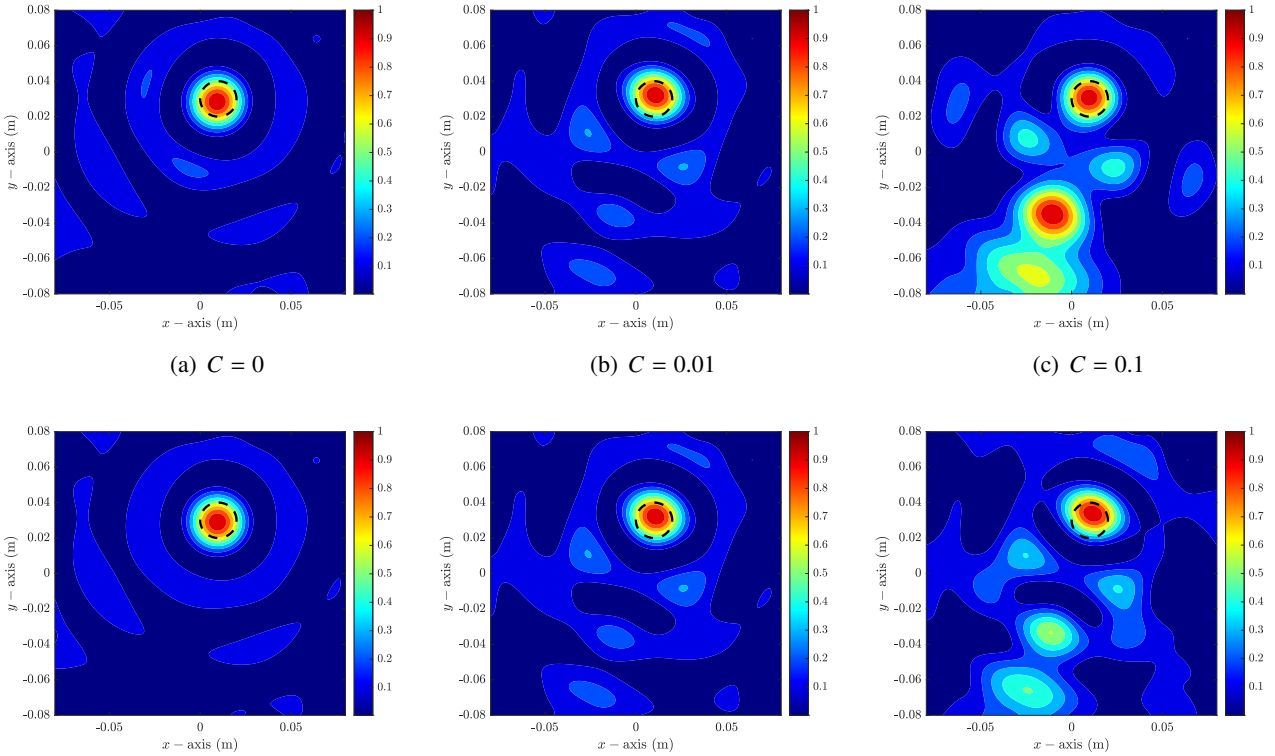

(a) $C = 0$ (b) $C = 0.01$ (c) $C = 0.1$

(d) $C = 0.001i$ (e) $C = 0.01i$ (f) $C = 0.1i$

Figure 3. (Example 4.1) Maps of $\mathfrak{F}(\mathbf{z}, C)$ at $f = 1$ GHz with various C. The black-colored dashed line describes the ∂D_1.

Figure 4 shows the distribution of singular values of $\mathbb{K}(C)$ for different C. Here, it is possible to distinguish between nonzero singular values τ_1 and τ_2 when $C = 0$ and $C = 0.001i$. However, if the value of $|C|$ is not near zero, it is very difficult to distinguish between nonzero and near zero singular values. To define the imaging function, we chose τ_1 as the nonzero singular value of $\mathbb{K}(C)$ for $C = 0.01$, $C = 0.01i$, and $0.1i$. For $C = 0.1$, we chose the first six τ_n as nonzero singular values.

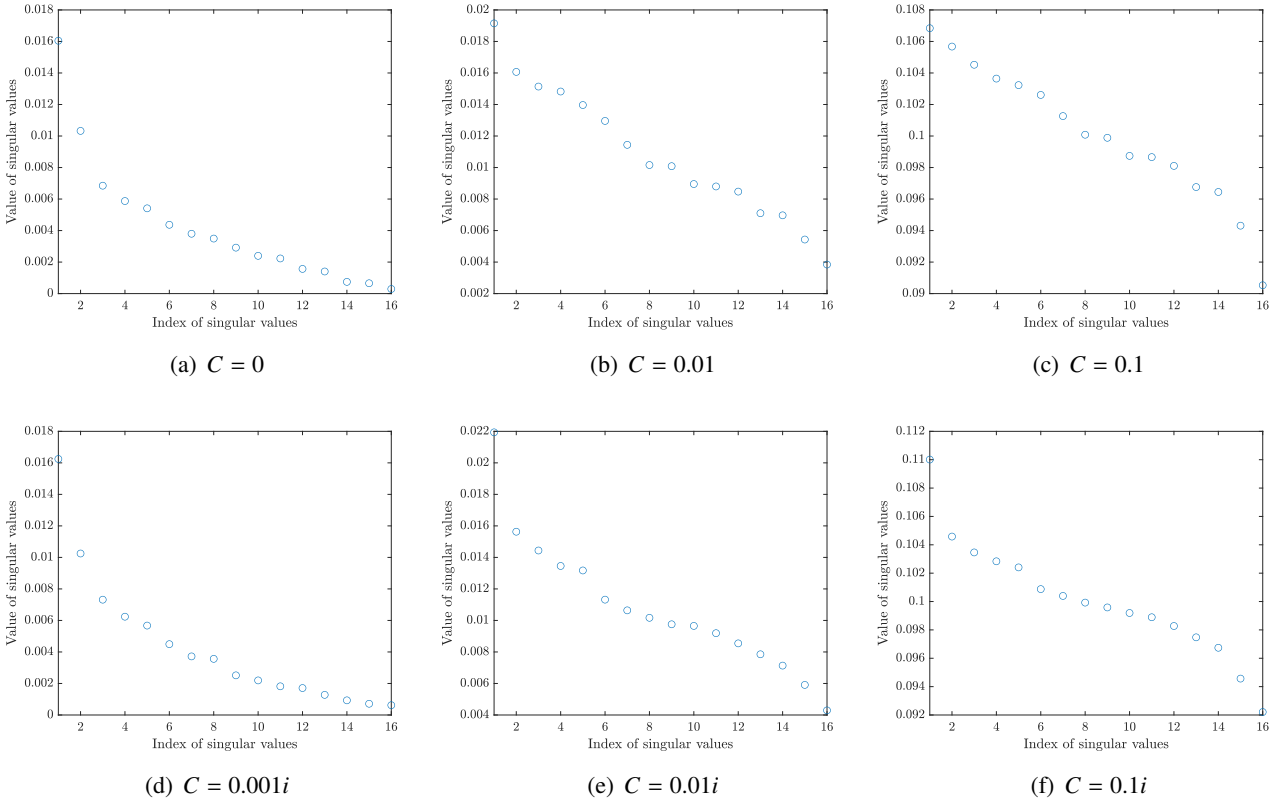

(a) $C = 0$ (b) $C = 0.01$ (c) $C = 0.1$

(d) $C = 0.001i$ (e) $C = 0.01i$ (f) $C = 0.1i$

Figure 4. (Example 4.2) Distribution of the singular values of $\mathbb{K}(C)$ at $f = 1\,\text{GHz}$ with various C.

Figure 5 displays the maps of $\mathfrak{F}(\mathbf{z}, C)$ for different C. Similar to single object imaging, the locations and shapes of D_1 and D_2 can be identified precisely through the map of $\mathfrak{F}(\mathbf{z}, C)$ when $C = 0, 0001i$, and $0.01i$. Moreover, it is possible to recognize D_1 and D_2, but the imaging result contains several artifacts with small magnitudes if $C = 0.01i$ and $C = 0.1i$. Unfortunately, it is difficult to distinguish D_1 and D_2 from several artifacts of large magnitudes if $C = 0.1$. Therefore, similar to the single object imaging, the imaging result of $\mathfrak{F}(\mathbf{z}, C)$ heavily depends on the choice of C. Additionally, good results can be obtained when $C = 0$ or $|C|$ is small enough to identify multiple objects.

Example 4.3 (Imaging of large object). Although equation (2.2) holds for small objects, we now use the $\mathfrak{F}(\mathbf{z}, C)$ to retrieve a large object. Figures 6 and 7 show the distribution of singular values of $\mathbb{K}(C)$ and corresponding imaging results of $\mathbb{K}(C)$ in the presence of a circular object with radius $\alpha = 0.048\,\text{m}$ and material properties $(\varepsilon, \sigma) = (15\varepsilon_0, 0.5\,\text{S/m})$. Similar to the previous results in Examples 4.1 and 4.2, it is possible to recognize the outline shape of an object if $C = 0$ and $C = 0.001i$, i.e., if the value of $|C|$ is very small. However, it is impossible to identify the object if $|C|$ is not small enough ($|C| \geq 0.01$ in this example).

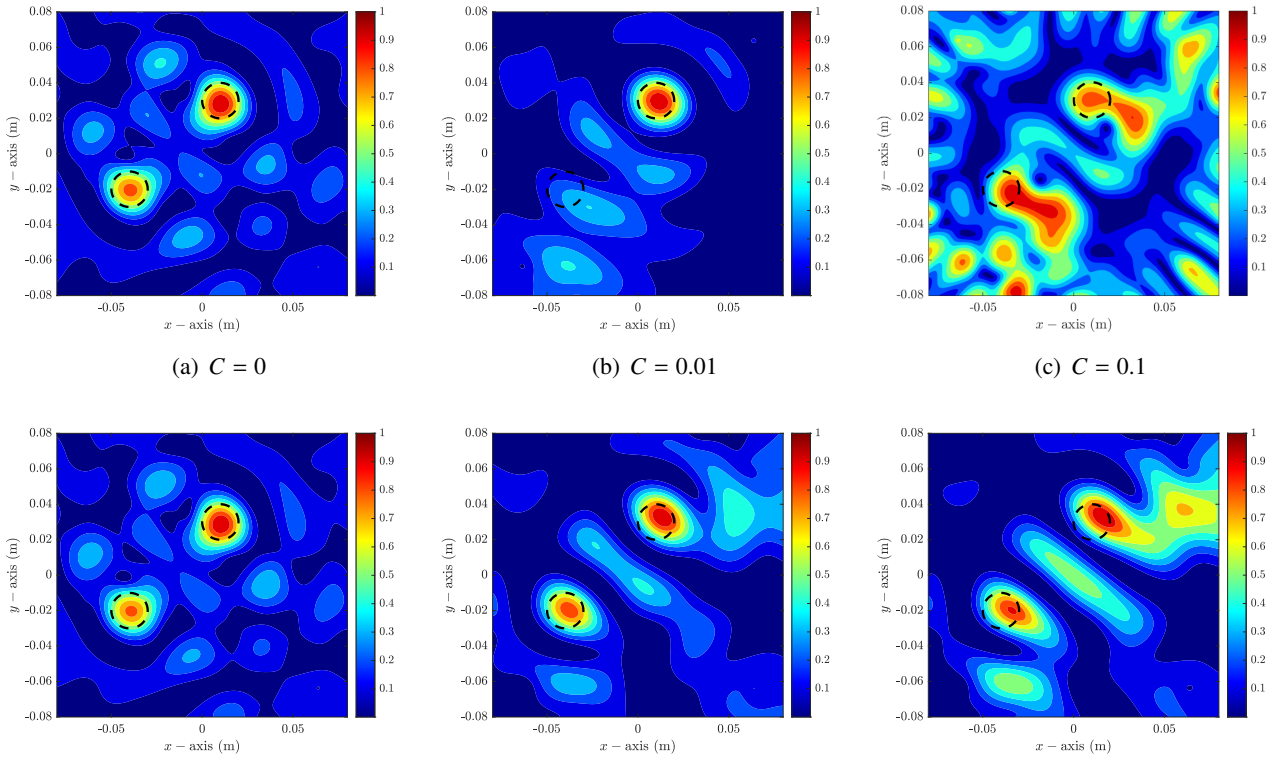

(a) $C = 0$ (b) $C = 0.01$ (c) $C = 0.1$

(d) $C = 0.001i$ (e) $C = 0.01i$ (f) $C = 0.1i$

Figure 5. (Example 4.2) Maps of $\Im(\mathbf{z}, C)$ at $f = 1$ GHz with various C. Black-colored dashed lines describe $\partial D_1 \cup \partial D_2$.

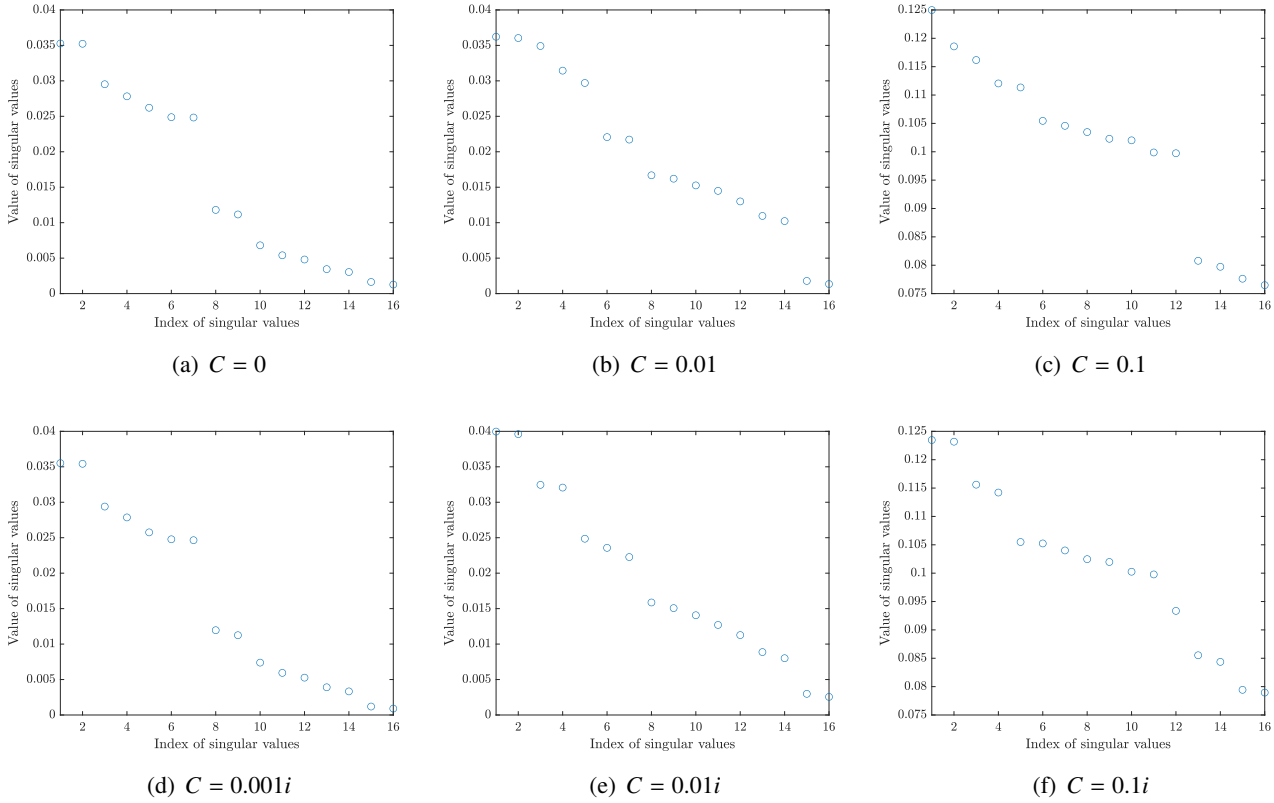

(a) $C = 0$ (b) $C = 0.01$ (c) $C = 0.1$

(d) $C = 0.001i$ (e) $C = 0.01i$ (f) $C = 0.1i$

Figure 6. (Example 4.3) Distribution of the singular values of $\mathbb{K}(C)$ at $f = 1\,\text{GHz}$ with various C.

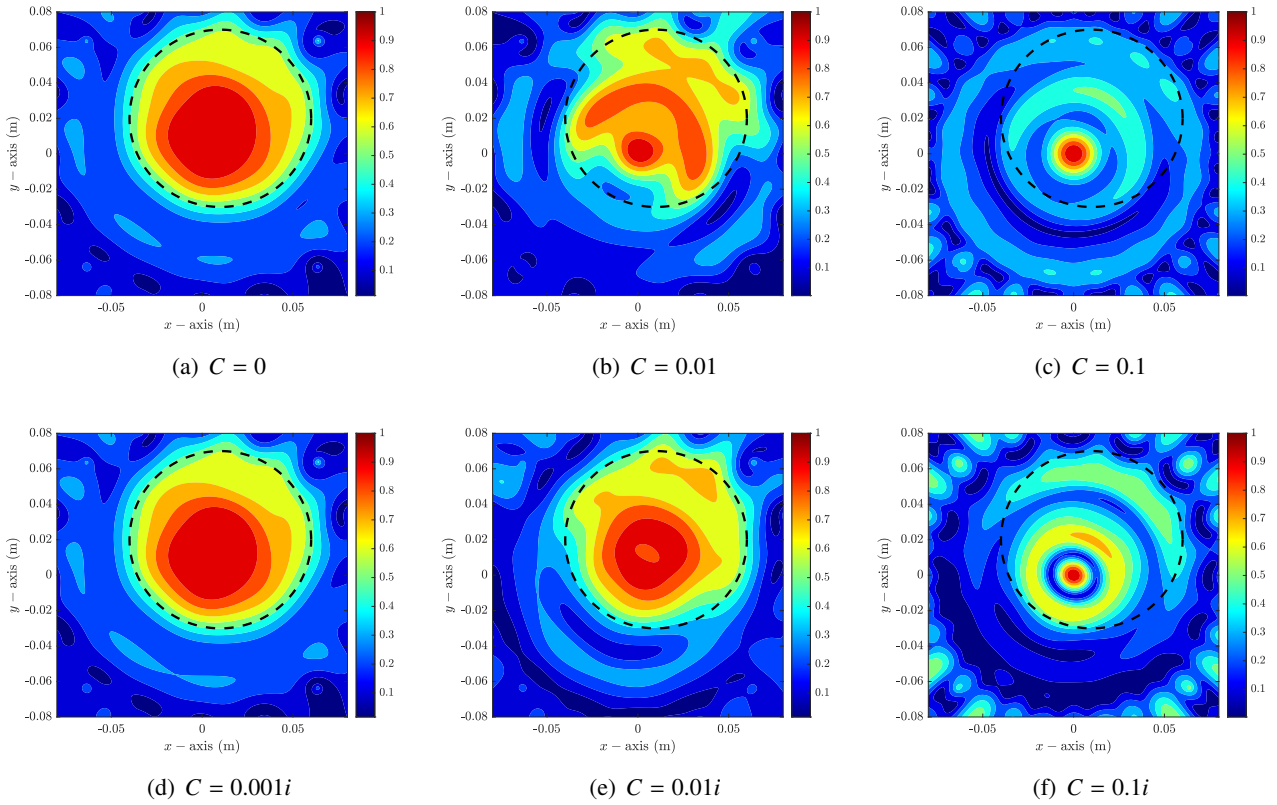

(a) $C = 0$ (b) $C = 0.01$ (c) $C = 0.1$

(d) $C = 0.001i$ (e) $C = 0.01i$ (f) $C = 0.1i$

Figure 7. (Example 4.3) Maps of $\mathfrak{F}(\mathbf{z}, C)$ at $f = 1$ GHz with various C. The black-colored dashed line describes ∂D.

4.2. Simulation results with experimental data

We now apply the imaging function of (2.7) to identify small objects and illustrate the effect of the converted constant C. To this end, the scattering matrix was constructed using the microwave machine, which was filled with water, and manufactured by the research group of the Electronics and Telecommunications Research Institute, see [4]. The ROI Ω was selected as the interior of a circular region centered at the origin with radius 0.085 m and material properties $(\varepsilon_b, \sigma_b) = (78\varepsilon_0, 0.2\,\mathrm{S/m})$ at $f = 925$ MHz. We refer to Figure 8 for illustrations of the microwave machine and selected objects (cross section of screwdrivers, hand hammer, and plastic straw).

Example 4.4 (Imaging of small objects with same material properties). Here, we consider the imaging of the cross section of screwdrivers D_s, where $s = 1, 2, 3$. Figure 9 illustrates the distribution of singular values of $\mathbb{K}(C)$ for different C. Similar to the synthetic data experiment (Example 4.1), it is simple to choose the first three singular values to define the imaging function when $C = 0$, 0.01, $0.001i$, and $0.01i$. However, it is difficult to choose nonzero singular values when $C = 0.1$ and $C = 0.1i$.

Figure 10 displays the maps of $\mathfrak{F}(\mathbf{z}, C)$ for different C. Similar to the results in Example 4.1, the existence, location, and outline shape of objects can be identified very accurately through the map of $\mathfrak{F}(\mathbf{z}, C)$, but some artifacts are included in the map when $|C| = 0.01$. Unfortunately, identifying some objects when $C = 0.1$ is extremely difficult, as is distinguishing between objects and artifacts of large magnitude when $C = 0.1i$. As with synthetic data experiments, the imaging result of $\mathfrak{F}(\mathbf{z}, C)$ is highly

dependent on the choice of C, and good results can be obtained when $|C|$ is small enough to identify small objects.

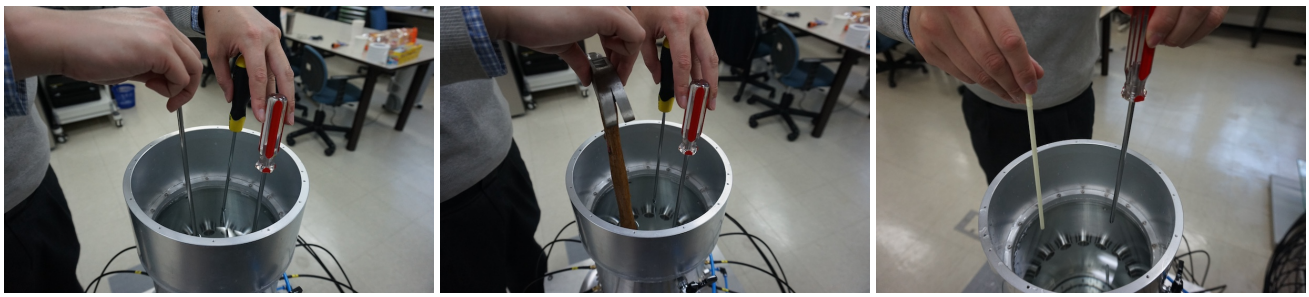

(a) three screwdrivers (b) hand hammer and screwdrivers (c) screwdriver and plastic straw

Figure 8. Pictures of real-data experiments for Examples 4.4 (left), 4.5 (center), and 4.6 (right).

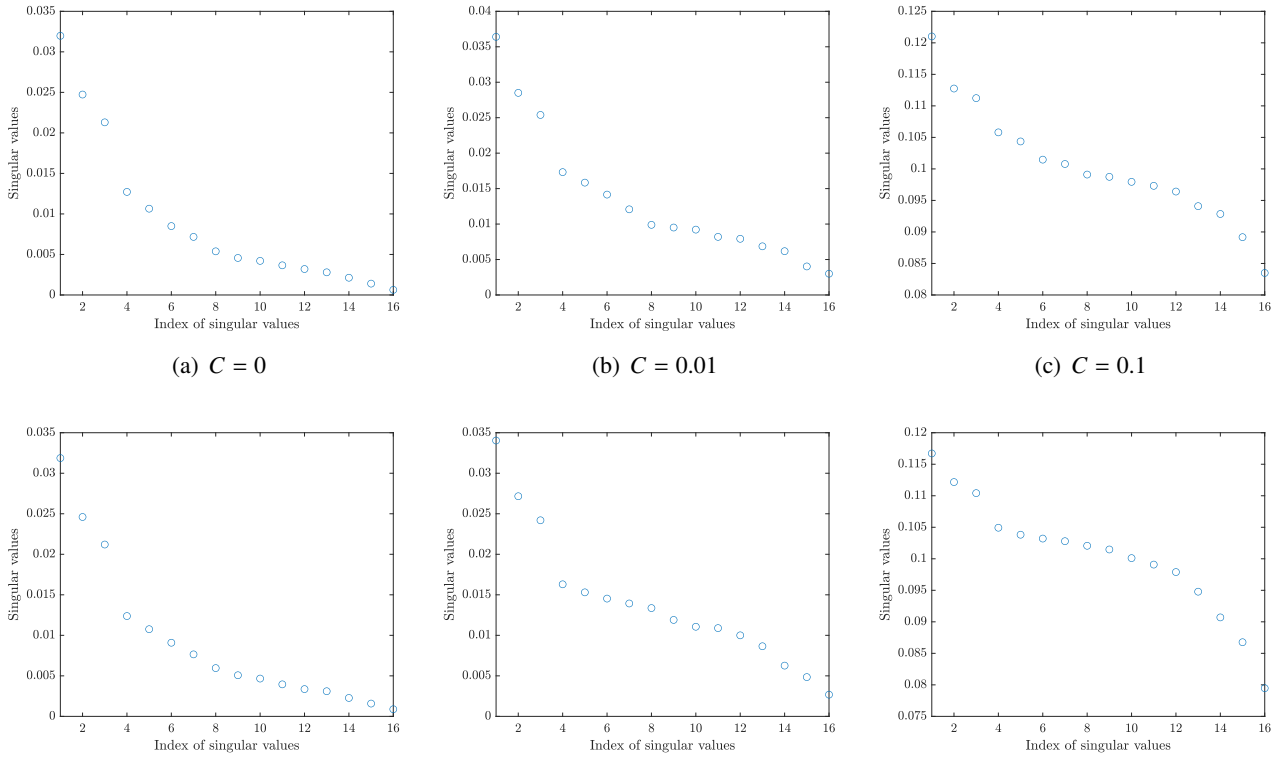

(a) $C = 0$ (b) $C = 0.01$ (c) $C = 0.1$

(d) $C = 0.001i$ (e) $C = 0.01i$ (f) $C = 0.1i$

Figure 9. (Example 4.4) Distribution of the singular values of $\mathbb{K}(C)$ at $f = 925\,\text{MHz}$ with various C.

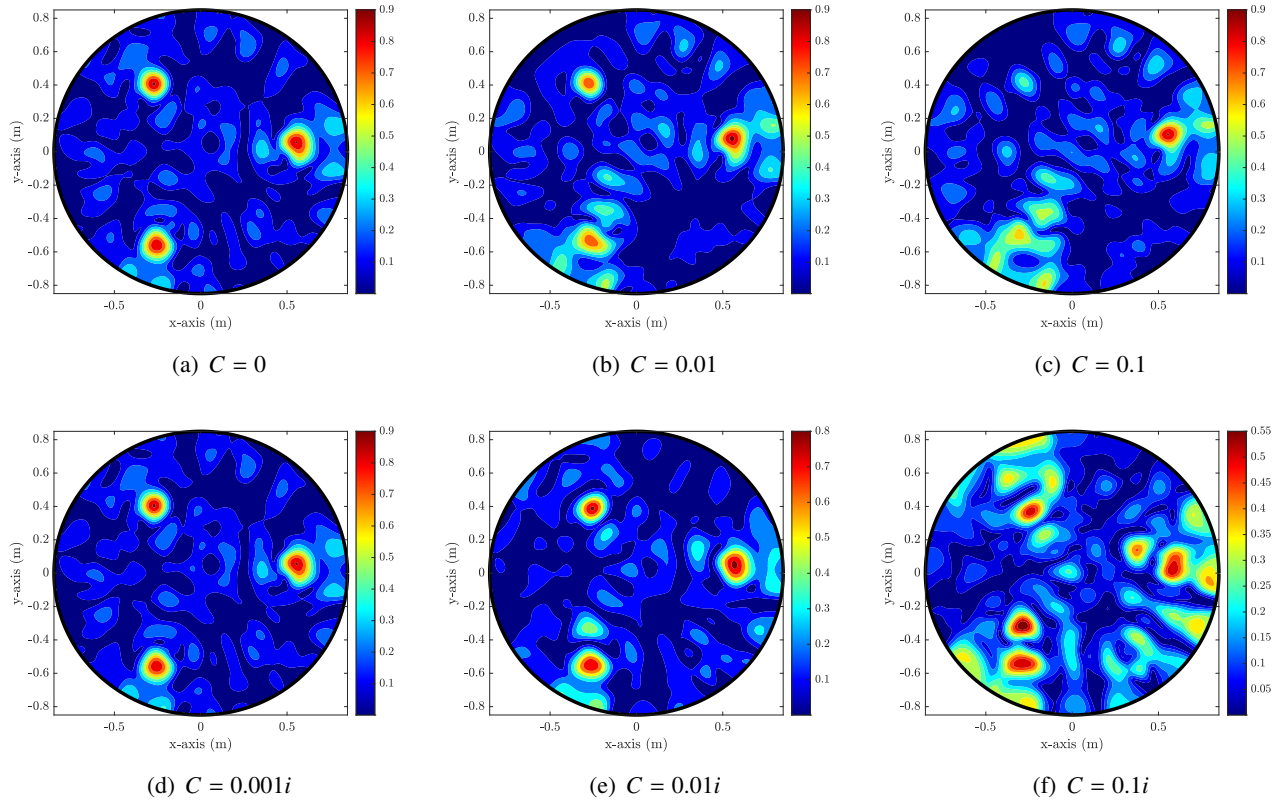

(a) $C = 0$ (b) $C = 0.01$ (c) $C = 0.1$

(d) $C = 0.001i$ (e) $C = 0.01i$ (f) $C = 0.1i$

Figure 10. (Example 4.4) Maps of $\mathfrak{F}(\mathbf{z}, C)$ at $f = 925$ MHz with various C.

Example 4.5 (Imaging of small objects with different sizes and shapes). Now, we exhibit a result for identifying the cross section of two screwdrivers and a hand hammer. Figure 11 exhibits the distribution of singular values of $\mathbb{K}(C)$ for different C. Same as in Example 4.4, it is easy to select nonzero singular values to define the imaging function when $C = 0$, 0.01, $0.001i$, and $0.01i$, but it is difficult to select when $C = 0.1$ and $C = 0.1i$.

Figure 12 shows the maps of $\mathfrak{F}(\mathbf{z}, C)$ for different C. Fortunately, it is possible to distinguish the cross section of hand hammer, which is larger than the cross section of screwdrivers if C is small enough. However, it is very difficult to recognize small objects when $C = 0.1i$ and distinguish small and large objects when $C = 0.1$.

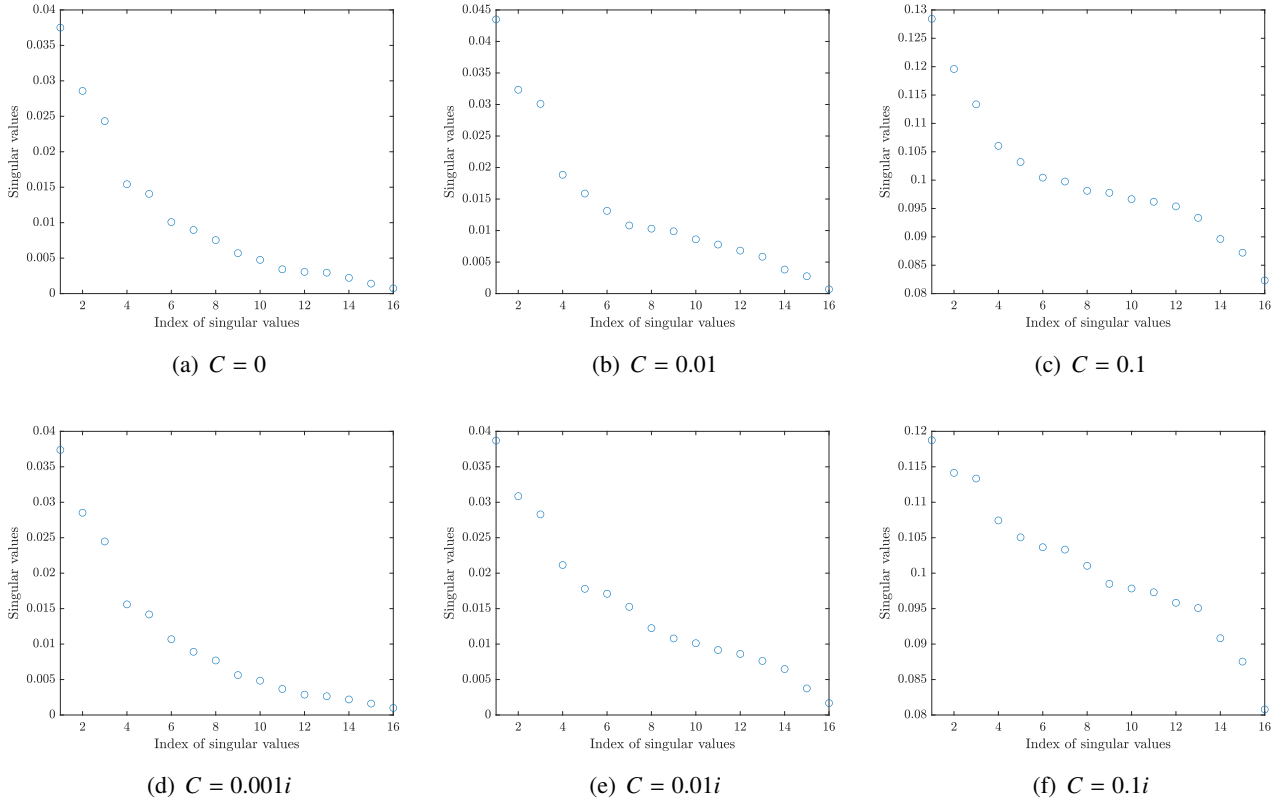

(a) $C = 0$ (b) $C = 0.01$ (c) $C = 0.1$

(d) $C = 0.001i$ (e) $C = 0.01i$ (f) $C = 0.1i$

Figure 11. (Example 4.5) Distribution of the singular values of $\mathbb{K}(C)$ at $f = 925$ MHz with various C.

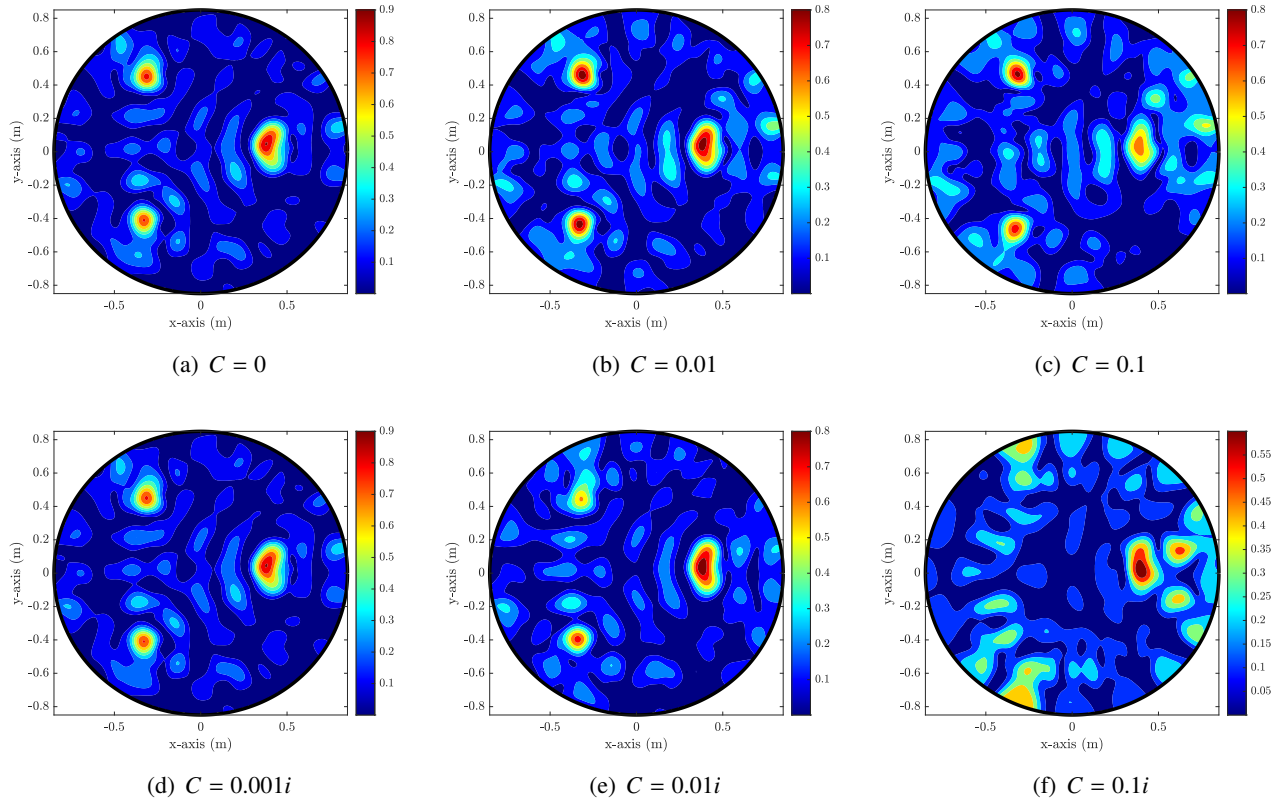

(a) $C = 0$ (b) $C = 0.01$ (c) $C = 0.1$

(d) $C = 0.001i$ (e) $C = 0.01i$ (f) $C = 0.1i$

Figure 12. (Example 4.5) Maps of $\mathfrak{F}(\mathbf{z}, C)$ at $f = 925$ MHz with various C.

Example 4.6 (Imaging of small objects with different material properties). For the final example, we show a result for identifying the cross section of a screwdriver and a plastic straw. Similar to the previous result in Example 4.4, it is not difficult to select a nonzero singular value when $C = 0$, 0.01, $0.001i$, and $0.01i$, but it is still difficult to select when $C = 0.1$ and $C = 0.1i$, refer to Figure 13. In this case, we selected τ_1 as the nonzero singular value of $\mathbb{K}(C)$, considering differences $\tau_n - \tau_{n+1}$, $n = 1, 2, \ldots, 15$. It is worth noting that the values of permittivity of the plastic straw and screwdriver are extremely low and high, respectively, and the existence of the plastic straw does not affect $\mathcal{S}_{\text{meas}}(n, m)$ because the value of O_D of (2.4) for the screwdriver is significantly larger than that of plastic straw. Correspondingly, only one singular value of $\mathbb{K}(C)$ that is significantly larger than the others has been observed.

Figure 14 displays the maps of $\mathfrak{F}(\mathbf{z}, C)$ for different C. Unlike previous results, the location and outline shape of the cross section of a screwdriver can be identified correctly through the map of $\mathfrak{F}(\mathbf{z}, C)$ with $|C| \leq 0.1$. Unfortunately, the screwdriver's cross section cannot be recognized for any value C.

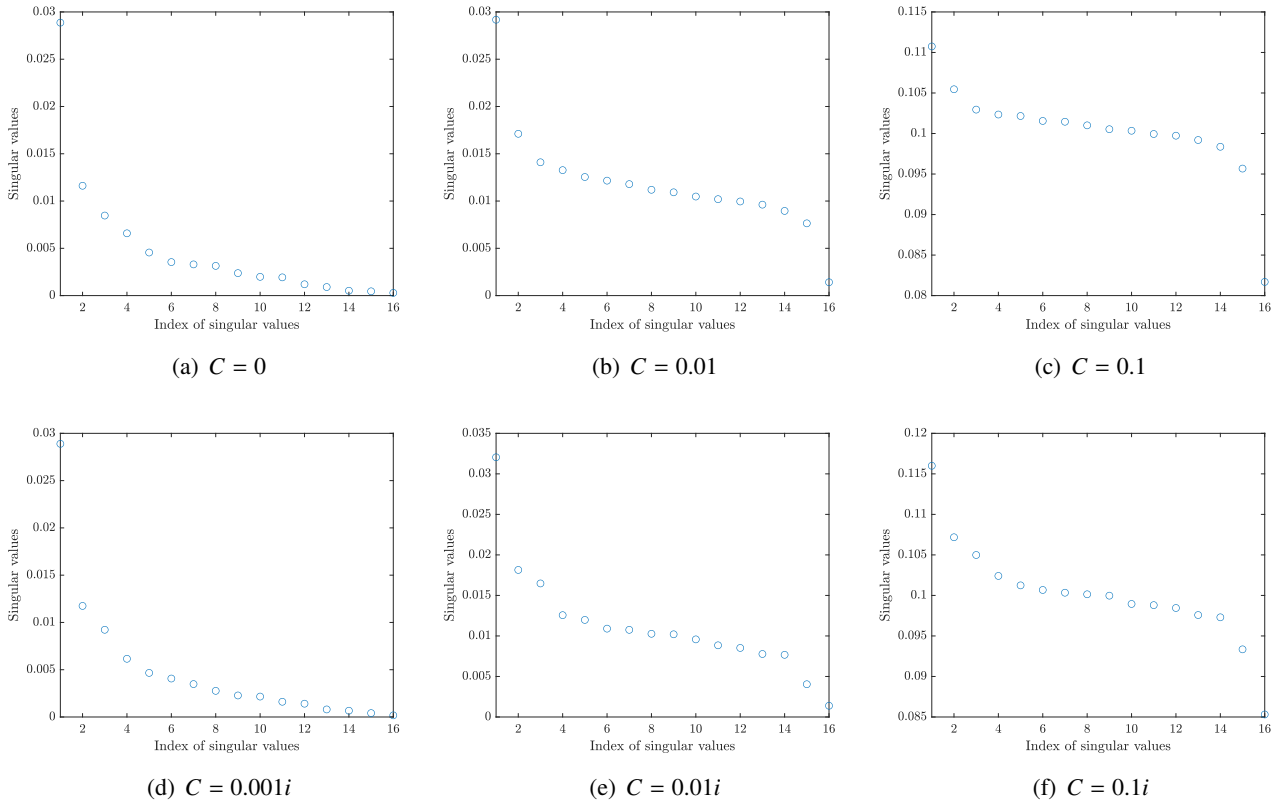

(a) $C = 0$ (b) $C = 0.01$ (c) $C = 0.1$

(d) $C = 0.001i$ (e) $C = 0.01i$ (f) $C = 0.1i$

Figure 13. (Example 4.6) Distribution of the singular values of $\mathbb{K}(C)$ at $f = 925$ MHz with various C.

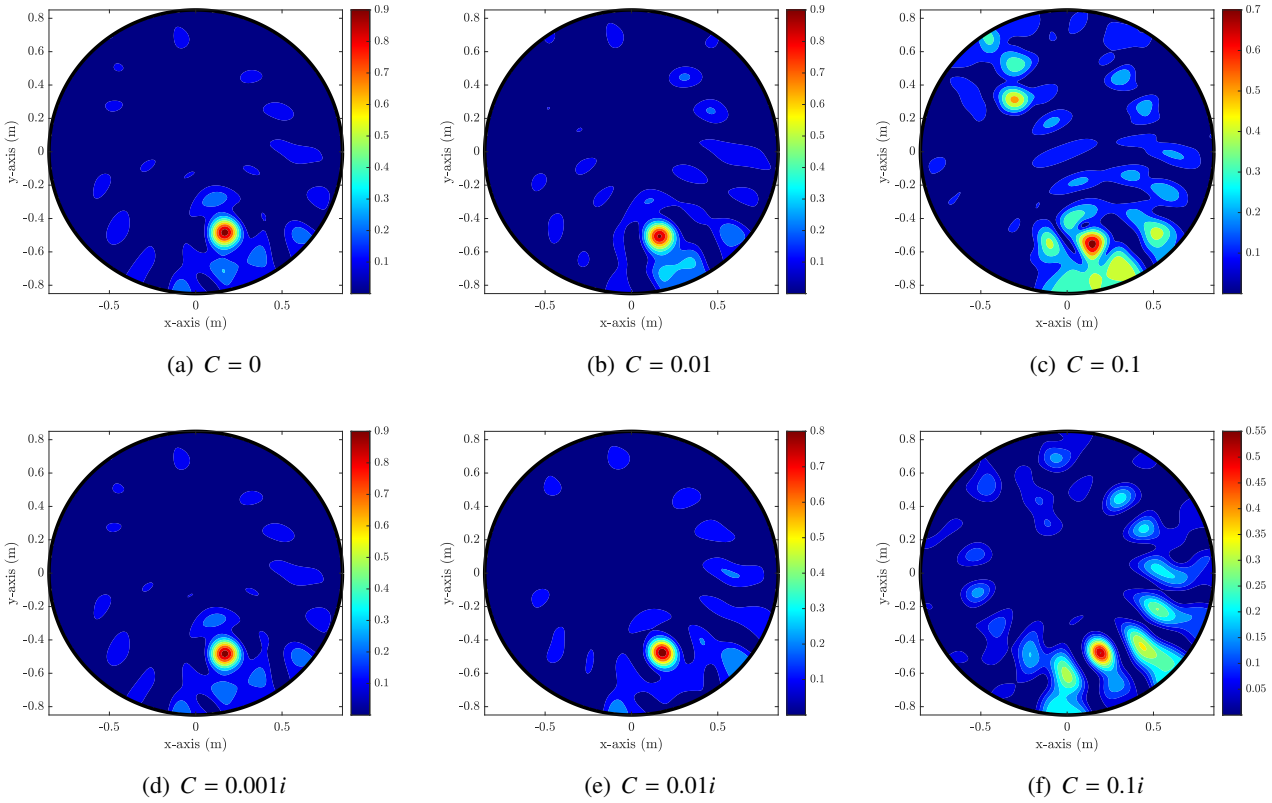

(a) $C = 0$ (b) $C = 0.01$ (c) $C = 0.1$

(d) $C = 0.001i$ (e) $C = 0.01i$ (f) $C = 0.1i$

Figure 14. (Example 4.6) Maps of $\Im(\mathbf{z}, C)$ at $f = 925$ MHz with various C.

Based on Theorem 3.1, Remark 3.1, and the simulation results, we can conclude that applying a small value of $|C|$ guarantees good imaging results. However, the criteria for *small value* is unclear. Hence, converting unknown diagonal data to $C = 0$ will be the best choice for properly applying the SM. This is the theoretical reason why most studies converted unknown measurement data to the zero constant as we discussed in Remark 3.1.

5. Conclusions

In this study, we investigated the use of SM for the rapid identification of small objects by converting unknown diagonal elements of the scattering matrix into a constant. We demonstrated the effectiveness of this approach by showing that the imaging function can be represented by an infinite series of Bessel functions of integer order, antenna number and arrangement, and an applied constant. Furthermore, we demonstrated that small object can be uniquely retrieved when the absolute value of the applied constant is zero or near zero.

It is important to note that the scope of this paper's analysis and application is limited to retrieving a small object in two dimensions. However, future research focusing on identifying large objects and expanding to three-dimensional microwave imaging would provide intriguing research topics. Finally, motivated by remarkable studies in regard to machine learning techniques [50–52], generating diagonal elements of scattering matrix will be also a remarkable research topic.

Use of AI tools declaration

The author declares he has not used Artificial Intelligence (AI) tools in the creation of this article.

Acknowledgments

The author would like to acknowledge two anonymous referees for their comments that help to increase the quality of the paper. This work was supported by the National Research Foundation of Korea (NRF) grant funded by the Korean government (MSIT) (NRF-2020R1A2C1A01005221) and the research program of Kookmin University.

Conflict of interest

The authors declare that there are no conflicts of interest associated with the publication of this paper.

Author contributions

Won-Kwang Park: Conceptualization, Formal Analysis, Investigation, Methodology, Software, Validation, Writing - Original Draft, Writing - Review & Editing, Funding acquisition.

References

1. H. Ammari, *An Introduction to Mathematics of Emerging Biomedical Imaging*, vol. 62 of Mathematics and Applications Series, Springer, Berlin, 2008. https://doi.org/10.1007/978-3-540-79553-7
2. R. Chandra, A. J. Johansson, M. Gustafsson, F. Tufvesson, A microwave imaging-based technique to localize an in-body RF source for biomedical applications, *IEEE T. Bio-Med. Eng.*, **62** (2015), 1231–1241. https://doi.org/10.1109/TBME.2014.2367117
3. M. Haynes, J. Stang, M. Moghaddam, Real-time microwave imaging of differential temperature for thermal therapy monitoring, *IEEE T. Bio-Med. Eng.*, **61** (2014), 1787–1797. https://doi.org/10.1109/TBME.2014.2307072
4. J. Y. Kim, K. J. Lee, B. R. Kim, S. I. Jeon, S. H. Son, Numerical and experimental assessments of focused microwave thermotherapy system at 925MHz, *ETRI J.*, **41** (2019), 850–862. https://doi.org/10.4218/etrij.2018-0088
5. L. Collins, P. Gao, D. Schofield, J. Moulton, L. Majakowsky, L. Reidy, et al.,

   A statistical approach to landmine detection using broadband electromagnetic data, *IEEE T. Geosci. Remote*, **40** (2002), 950–962. https://doi.org/10.1109/TGRS.2002.1006387
6. P. Gao, L. Collins, P. M. Garber, N. Geng, L. Carin, Classification of landmine-like metal targets using wideband electromagnetic induction, *IEEE T. Geosci. Remote Sens.*, **38** (2000), 1352–1361. https://doi.org/10.1109/ICASSP.1999.758404

7. Y. J. Kim, L. Jofre, F. D. Flaviis, M. Q. Feng, Microwave reflection tomographic array for damage detection of civil structures, *IEEE T. Antenn. Propag.*, **51** (2003), 3022–3032. https://doi.org/10.1109/TAP.2003.818786
8. C. B. Smith, E. M. Hernandez, Non-negative constrained inverse eigenvalue problems–application to damage identification, *Mech. Syst. Signal Proc.*, **129** (2019), 629–644. https://doi.org/10.1016/j.ymssp.2019.04.052
9. V. S. Chernyak, *Fundamentals of Multisite Radar Systems: Multistatic Radars and Multiradar Systems*, CRC Press, Routledge, 1998. https://doi.org/10.1201/9780203755228
10. I. Stojanovic, W. C. Karl, Imaging of moving targets with multi-static SAR using an overcomplete dictionary, *IEEE J.-STSP.*, **4** (2010), 164–176. https://doi.org/10.1109/JSTSP.2009.2038982
11. T. Rubæk, P. M. Meaney, P. Meincke, K. D. Paulsen, Nonlinear microwave imaging for breast-cancer screening using Gauss–Newton's method and the CGLS inversion algorithm, *IEEE T. Antenn. Propag.*, **55** (2007), 2320–2331. https://doi.org/10.1109/TAP.2007.901993
12. D. Ireland, K. Bialkowski, A. Abbosh, Microwave imaging for brain stroke detection using Born iterative method, *IET Microw. Antenna. P.*, **7** (2013), 909–915. https://doi.org/10.1049/iet-map.2013.0054
13. G. Oliveri, N. Anselmi, A. Massa, Compressive sensing imaging of non-sparse 2D scatterers by a total-variation approach within the Born approximation, *IEEE T. Antenn. Propag.*, **62** (2014), 5157–5170. https://doi.org/10.1109/TAP.2014.2344673
14. A. Franchois, C. Pichot, Microwave imaging-complex permittivity reconstruction with a Levenberg-Marquardt method, *IEEE T. Antenn. Propag.*, **45** (1997), 203–215. https://doi.org/10.1109/8.560338
15. O. Dorn, D. Lesselier, Level set methods for inverse scattering, *Inverse Probl.*, **22** (2006), R67–R131. https://doi.org/10.1088/0266-5611/22/4/R01
16. O. Kwon, J. K. Seo, J. R. Yoon, A real-time algorithm for the location search of discontinuous conductivities with one measurement, *Comm. Pur. Appl. Math.*, **55** (2002), 1–29. https://doi.org/10.1002/cpa.3009
17. W. K. Park, D. Lesselier, Reconstruction of thin electromagnetic inclusions by a level set method, *Inverse Probl.*, **25** (2009), Article No. 085010. https://doi.org/10.1088/0266-5611/25/8/085010
18. S. H. Son, W. K. Park, Application of the bifocusing method in microwave imaging without background information, *J. Korean Soc. Ind. Appl. Math.*, **27** (2023), 109–122. https://doi.org/10.12941/jksiam.2023.27.109
19. H. Ammari, H. Kang, E. Kim, K. Louati, M. Vogelius, A MUSIC-type algorithm for detecting internal corrosion from electrostatic boundary measurements, *Numer. Math.*, **108** (2008), 501–528. https://doi.org/10.1007/s00211-007-0130-x
20. W. K. Park, Application of MUSIC algorithm in real-world microwave imaging of unknown anomalies from scattering matrix, *Mech. Syst. Signal Proc.*, **153** (2021), Article No. 107501. https://doi.org/10.1016/j.ymssp.2020.107501
21. Y. T. Chow, K. Ito, K. Liu, J. Zou, Direct sampling method for diffusive optical tomography, *SIAM J. Sci. Comput.*, **37** (2015), A1658–A1684. https://doi.org/10.1137/14097519X

22. Y. T. Chow, K. Ito, J. Zou, A direct sampling method for electrical impedance tomography, *Inverse Probl.*, **30** (2014), Article No. 095003. https://doi.org/10.1088/0266-5611/30/9/095003

23. S. Amstutz, N. Dominguez, Topological sensitivity analysis in the context of ultrasonic non-destructive testing, *Eng. Anal. Bound. Elem.*, **32** (2008), 936–947. https://doi.org/10.1016/j.enganabound.2007.09.008

24. F. L. Louër, M. L. Rapún, Detection of multiple impedance obstacles by non-iterative topological gradient based methods, *J. Comput. Phys.*, **388** (2019), 534–560. https://doi.org/10.1016/j.jcp.2019.03.023

25. W. K. Park, A novel study on the orthogonality sampling method in microwave imaging without background information, *Appl. Math. Lett.*, **145** (2023), Article No. 108766. https://doi.org/10.1016/j.aml.2023.108766

26. T. Le, D. L. Nguyen, H. Schmidt, T. Truong, Imaging of 3D objects with experimental data using orthogonality sampling methods, *Inverse Probl.*, **38** (2021), Article No. 025007. https://doi.org/10.1088/1361-6420/ac3d85

27. S. Coşğun, E. Bilgin, M. Çayören, Microwave imaging of breast cancer with factorization method: SPIONs as contrast agent, *Med. Phys.*, **47** (2020), 3113–3122. https://doi.org/10.1002/mp.14156

28. B. Harrach, J. K. Seo, E. J. Woo, Factorization method and its physical justification in frequency-difference electrical impedance tomography, *IEEE T. Biomed. Eng.*, **29** (2010), 1918–1926. https://doi.org/10.1109/tmi.2010.2053553

29. H. F. Alqadah, A compressive multi-frequency linear sampling method for underwater acoustic imaging, *IEEE T. Image Process.*, **25** (2016), 2444–2455. https://doi.org/10.1109/TIP.2016.2548243

30. M. G. Aram, M. Haghparast, M. S. Abrishamian, A. Mirtaheri, Comparison of imaging quality between linear sampling method and time reversal in microwave imaging problems, *Inverse Probl. Sci. Eng.*, **24** (2016), 1347–1363. https://doi.org/10.1080/17415977.2015.1104308

31. H. Ammari, J. Garnier, H. Kang, M. Lim, K. Sølna, Multistatic imaging of extended targets, *SIAM J. Imag. Sci.*, **5** (2012), 564–600. https://doi.org/10.1137/10080631X

32. L. Borcea, G. Papanicolaou, F. G. Vasquez, Edge illumination and imaging of extended reflectors, *SIAM J. Imag. Sci.*, **1** (2008), 75–114. https://doi.org/10.1137/07069290X

33. W. K. Park, On the identification of small anomaly in microwave imaging without homogeneous background information, *AIMS Math.*, **8** (2023), 27210–27226. https://doi.org/10.3934/math.20231392

34. H. Ammari, J. Garnier, H. Kang, W. K. Park, K. Sølna, Imaging schemes for perfectly conducting cracks, *SIAM J. Appl. Math.*, **71** (2011), 68–91. https://doi.org/10.1137/100800130

35. W. K. Park, Multi-frequency subspace migration for imaging of perfectly conducting, arc-like cracks in full- and limited-view inverse scattering problems, *J. Comput. Phys.*, **283** (2015), 52–80. https://doi.org/10.1016/j.jcp.2014.11.036

36. W. K. Park, Shape identification of open sound-hard arcs without priori information in limited-view inverse scattering problem, *Comput. Math. Appl.*, **128** (2022), 55–68. https://doi.org/10.1016/j.camwa.2022.10.010

37. W. K. Park, Fast location search of small anomaly by using microwave, *Int. J. Appl. Electromagn. Mech.*, **59** (2019), 1505–1510. https://doi.org/10.3233/JAE-171107

38. W. K. Park, Real-time microwave imaging of unknown anomalies via scattering matrix, *Mech. Syst. Signal Proc.*, **118** (2019), 658–674. https://doi.org/10.1016/j.ymssp.2018.09.012

39. W. K. Park, Real-time detection of small anomaly from limited-aperture measurements in real-world microwave imaging, *Mech. Syst. Signal Proc.*, **171** (2022), Article No. 108937. https://doi.org/10.1016/j.ymssp.2022.108937

40. S. H. Son, H. J. Kim, K. J. Lee, J. Y. Kim, J. M. Lee, S. I. Jeon, et al., Experimental measurement system for 3–6GHz microwave breast tomography, *J. Electromagn. Eng. Sci.*, **15** (2015), 250–257. https://doi.org/10.5515/JKIEES.2015.15.4.250

41. S. H. Son, K. J. Lee, W. K. Park, Real-time tracking of moving objects from scattering matrix in real-world microwave imaging, *AIMS Math.*, **9** (2024), 13570–13588. https://doi.org/10.3934/math.2024662

42. S. H. Son, N. Simonov, H. J. Kim, J. M. Lee, S. I. Jeon, Preclinical prototype development of a microwave tomography system for breast cancer detection, *ETRI J.*, **32** (2010), 901–910. https://doi.org/10.4218/etrij.10.0109.0626

43. S. Kang, W. K. Park, S. H. Son, A qualitative analysis of the bifocusing method for a real-time anomaly detection in microwave imaging, *Comput. Math. Appl.*, **137** (2023), 93–101. https://doi.org/10.1016/j.camwa.2023.02.017

44. K. J. Lee, S. H. Son, W. K. Park, A real-time microwave imaging of unknown anomaly with and without diagonal elements of scattering matrix, *Results Phys.*, **17** (2020), Article No. 103104. https://doi.org/10.1016/j.rinp.2020.103104

45. W. K. Park, On the application of orthogonality sampling method for object detection in microwave imaging, *IEEE T. Antenn. Propag.*, **71** (2023), 934–946. https://doi.org/10.1109/TAP.2022.3220033

46. S. H. Son, K. J. Lee, W. K. Park, Application and analysis of direct sampling method in real-world microwave imaging, *Appl. Math. Lett.*, **96** (2019), 47–53. https://doi.org/10.1016/j.aml.2019.04.016

47. M. Slaney, A. C. Kak, L. E. Larsen, Limitations of imaging with first-order diffraction tomography, *IEEE T. Microw. Theory*, **32** (1984), 860–874. https://doi.org/10.1109/TMTT.1984.1132783

48. D. Colton, R. Kress, *Inverse Acoustic and Electromagnetic Scattering Problems*, vol. 93 of Mathematics and Applications Series, Springer, New York, 1998. https://doi.org/10.1007/978-3-030-30351-8

49. L. J. Landau, Bessel functions: monotonicity and bounds, *J. London Math. Soc.*, **61** (2000), 197–215. https://doi.org/10.1112/S0024610799008352

50. M. H. Ding, H. Liu, G. H. Zheng, On inverse problems for several coupled PDF systems arising in mathematical biology, *J. Math. Biology*, **87** (2023), Article No. 86. https://doi.org/10.1007/s00285-023-02021-4

51. H. Liu, C. W. K. Lo, Determining a parabolic system by boundary observation of its non-negative solutions with biological applications, *Inverse Probl.*, **40** (2024), Article No. 025009. https://doi.org/10.1088/1361-6420/ad149f

52. Y. Yin, W. Yin, P. Meng, H. Liu, The interior inverse scattering problem for a two-layered cavity using the Bayesian method, *Inverse Probl. Imag.*, **16** (2022), 673–690. https://doi.org/10.3934/ipi.2021069

AIMS Press